Genesis of magmatic ilmenite ores associated with the Mazua ultramafic intrusion, NE Mozambique

doi: 10.1016/j.oregeorev.2022.104760

Ore Geology Reviews 143 (2022) 104760

Contents lists available at ScienceDirect

Ore Geology Reviews

journal homepage: www.elsevier.com/locate/oregeorev

Genesis of magmatic ilmenite ores associated with the Mazua ultramafic intrusion, NE Mozambique

David A.B. Unganai [a,b,*], Akira Imai [a,b], Ryohei Takahashi [b], Daud L. Jamal [c], Andrea Agangi [b], Takashi Hoshide [b], Hinako Sato [b]

[a] Department of Earth Resources Engineering, Kyushu University, Fukuoka 819-0395, Japan
[b] Department of Earth Resource Science, Akita University, Akita 010-8502, Japan
[c] Department of Geology, Eduardo Mondlane University, Maputo 257, Mozambique

ARTICLE INFO

Keywords:
Fe-Ti oxides
Ilmenite
Ultramafic intrusions
Mazua
Mozambique

ABSTRACT

The Mazua ultramafic intrusion is among the most promising intrusions hosting Fe-Ti oxide ores in Mozambique. Fe-Ti oxide ores are mainly composed of ilmenite occurring as lenses, veins and layers, either massive or disseminated in hornblende pyroxenite. This study discusses the nature and origin of the intrusion and related ilmenite ore body on the basis of whole-rock and mineral chemistry. Textural and structural evidences support a cumulate origin for these rocks, including the occurrence of relict cumulate textures, layering of alternating oxides and silicate-rich rocks, and size-grading of silicate-rich layers. Primary magmatic features have, however, largely been overprinted by subsolidus processes. The occurrence of the cumulate assemblage (Fe-Ti oxides and clinopyroxene), without plagioclase and olivine, suggests that the magma underwent differentiation before its emplacement. The evolved magmatic nature of the intrusion is consistent with the calculated Mg-number of approximately 50 for the melt in equilibrium with clinopyroxene crystals. The high TiO_2 concentrations (>4 wt %) of the evolved magma, by differentiation, are interpreted as the main factors controlling the crystallization of Fe-Ti oxides. We propose that the ores formed from crystallization and settling of Fe-Ti oxide minerals from an evolved basaltic magma. This model is consistent with (1) the occurrence of Fe-Ti oxides and clinopyroxene as cumulates in relation to the coexisting amphibole, (2) the layering structures of alternating oxides and silicate matrix, (3) the scarcity of apatite supported by the extremely low whole-rock P_2O_5 concentrations and (4) the restricted occurrence of ore veins, excluding the formation from immiscible oxide melts.

1. Introduction

Central and northern Mozambique are characterized by the occurrences of Fe-Ti oxide ore-hosting intrusions including the Tete Suite in the Tete Province and the Mazua ultramafic intrusion in the Nampula Province (Geological Institute Belgrade, 1984; Cílek, 1989; Lächelt, 2004). The geology, petrology, geochemistry, and geochronology of the Tete Suite are relatively well documented, although less work has been done on the Fe-Ti oxide mineralization (Barr and Brown, 1987; Evans et al., 1999; GTK Consortium, 2006; Westerhof et al., 2008). Magmatic Fe-Ti-V oxide ore deposits are commonly related to and hosted by anorthosite massifs and mafic–ultramafic intrusions (Duchesne, 1999; Zhou et al., 2005; Pang et al., 2008) and are less commonly associated with alkaline igneous complexes (e.g. Milani et al., 2017). The ores occur as disseminated oxides in the host rocks, layers or lenses and veins, which are commonly concordant with the host rocks (Pang et al., 2008; Charlier et al., 2015). In contrast to many mafic–ultramafic intrusions around the world (e.g. Bushveld Complex, Reynolds, 1985; Cawthorn and Ashwal, 2009), the Fe-Ti oxide deposit at Mazua belongs to an uncommon group of Fe-Ti oxide deposits, because ilmenite is the main ore mineral rather than titanomagnetite. The ore body at Mazua, discovered in the 1980s during an exploration campaign for asbestos, extends horizontally for 10 km and the calculated reserve of ilmenite up to a depth of 5 m is 2.7 million tons, associated with the so-called pyroxenite-amphibolite zone (Geological Institute Belgrade, 1984; Cílek, 1989).

Geological Institute Belgrade (1984) provided descriptions of the ilmenite body at Mazua and Cílek (1989) suggested a probable genetic link with unknown anorthosite-gabbro bodies. A magmatic origin of the ilmenite body was further supported by Lächelt (2004), who suggested that the ilmenite body at Mazua was associated with the Tete Suite.

* Corresponding author at: Department of Earth Resources Engineering, Kyushu University, 744 Motooka, Nishi-ku, Fukuoka 819-0395, Japan.
E-mail address: dabubene@gmail.com (D.A.B. Unganai).

https://doi.org/10.1016/j.oregeorev.2022.104760
Received 25 September 2021; Received in revised form 31 January 2022; Accepted 6 February 2022
Available online 10 February 2022

Norconsult Consortium (2007) reported whole-rock geochemical results of two samples of the host rocks with an average grade of up to 27 wt% TiO_2, 35 wt% FeO_{Total}, and ~ 2000 ppm V. In 2011, following the mineral potential described by Geological Institute Belgrade (1984), an Australian company (Globe Metals & Mining) carried out an Fe-Ti exploration program in the Mazua area, which culminated with the opening of several trenches in the study area. These trenches served as sampling points for this study. Mandlaze (2013) mapped part of the Mazua area producing a 1:10,000 scale geological map, and also presented a preliminary petrological study of the rocks from the area. The present study is the first comprehensive documentation of the origin and evolution of the Mazua ultramafic intrusion on the basis of new chemical analyses on whole-rock and mineral composition with an aim to constrain the nature and origin of the Mazua ultramafic intrusion and associated ilmenite ore body.

2. Geological background

2.1. Geological setting

Northeastern Mozambique lies in the Mozambique Belt, a southern part of the East African Orogen (EAO) (Fig. 1). Paleogeographic reconstructions of Gondwana suggest that Northeastern Mozambique is situated at the critical intersection of significant Pan-African orogenic belts (Fig. 1a; Viola et al., 2008; Engvik et al., 2019). These orogenic belts include (1) the N-S-trending East African Orogen; (2) the E-W-trending Zambezi Belt; (3) Dronning Maud Province in Eastern Antarctica; and (4) the Lützow-Holm Complex and Prydz Bay Belt, Antarctica (Viola et al., 2008; Engvik et al., 2019). The EAO is the world's largest Neoproterozoic to Cambrian mobile belt (Stern, 1994), extending from southern Israel, Sinai, and Jordan in the north to Mozambique and Madagascar in the south. The southern extension of the EAO into East Antarctica has been suggested by several researchers (e.g. Jacobs et al., 1998). The EAO was described as a crustal section that consists of a complex collage of individual oceanic domains and continental fragments between the Archean Sahara–Congo–Kalahari Cratons in the west and Neoproterozoic Indian terranes in the east (Fritz et al., 2013). Traditionally, the EAO is subdivided into two terrains based on lithological and metamorphic differences namely the upper crustal Arabian-Nubian Shield (ANS) and lower crustal Mozambique Belt (MB). The ANS is dominantly juvenile, being composed of abundant island-arc rocks and ophiolites, and is characterized by low-grade metamorphism (Kröner and Stern, 2004). On the other hand, the MB consists of medium- to high-grade gneisses and voluminous granitoids (Kröner and Stern, 2004). The protoliths of these assemblages consist predominantly of much older Archean to Mesoproterozoic continental crusts that were reworked during the Neoproterozoic (Stern, 1994; Kröner and Stern, 2004; Fritz et al., 2013). The overall model for the emplacement of MB is still under debate, although most researchers widely agree that the MB resulted from a Tibetan-style continent–continent collision between West Gondwana and East Gondwana (Kröner and Stern, 2004).

The crust of Northeastern Mozambique is composed of predominantly medium to high-grade rocks with Mesoproterozoic protolith ages (Norconsult Consortium, 2007; Macey et al., 2010). It is generally subdivided into a number of distinct megatectonic units based on their genetic differences (Norconsult Consortium, 2007; Viola et al., 2008; Macey et al., 2010): (1) The Paleoproterozoic domain, known as the Ponta Messuli Complex, consisting of migmatitic paragneisses, augen gneisses, talc schists, and amphibolites, forms the NW Ubendian-Usagaran foreland of the Pan-African orogen (Viola et al., 2008; Grantham et al., 2011; Engvik et al., 2019). (2) The Mesoproterozoic domain is very extensive and comprises the Nampula, Marrupa, Unango, Nairoto and Meluco Complexes (Viola et al., 2008; Grantham et al., 2011). The units are characterized mainly by granitic, granodioritic, tonalitic and banded migmatitic gneisses and are overprinted by granulite and upper amphibolite facies metamorphism and deformation, due to their tectonic and juxtaposition and reworking between 580 and 520 Ma (Engvik et al., 2007; Norconsult Consortium, 2007; Viola et al., 2008; Grantham et al., 2011). (3) The Mesoproterozoic terranes are overlain and deformed by Neoproterozoic crustal slices consisting of the Xixano, Lalamo, M'sawize, and Muaquia Complexes in addition to the Monapo and Mugeba klippen (Viola et al., 2008). These Neoproterozoic domains are known as the "Cabo Delgado Nappe Complex" and represent a "far-transported'' upper nappe system, emplaced northwestward during the Pan-African orogeny (Viola et al., 2008). The nappes are heterogeneous in their composition, comprising granitic, tonalitic, gabbroic, amphibolitic gneisses and various paragneisses, metavolcanics and mafic granulites (Norconsult Consortium, 2007; Viola et al., 2008). (4) The Nampula, Unango and Ponta Messuli Complexes are covered by localized Neoproterozoic supracrustal sequences namely the Mecubúri and the Alto Benfica Groups (overlying the Nampula Complex) consisting of metaconglomerates and biotite gneisses, the Geci Group (overlying the Unango Complex) characterized by metavolcanic rocks, conglomerates with pebbles of fine-grained granites, mica schists and limestones and the Txitonga Group (which might be overlying the Ponta Messuli Complex) dominated by metasedimentary rocks, mainly metagreywackes, metasandstones, quartz-mica schists, and chlorite-rich schists (Norconsult Consortium, 2007; Viola et al., 2008; Thomas

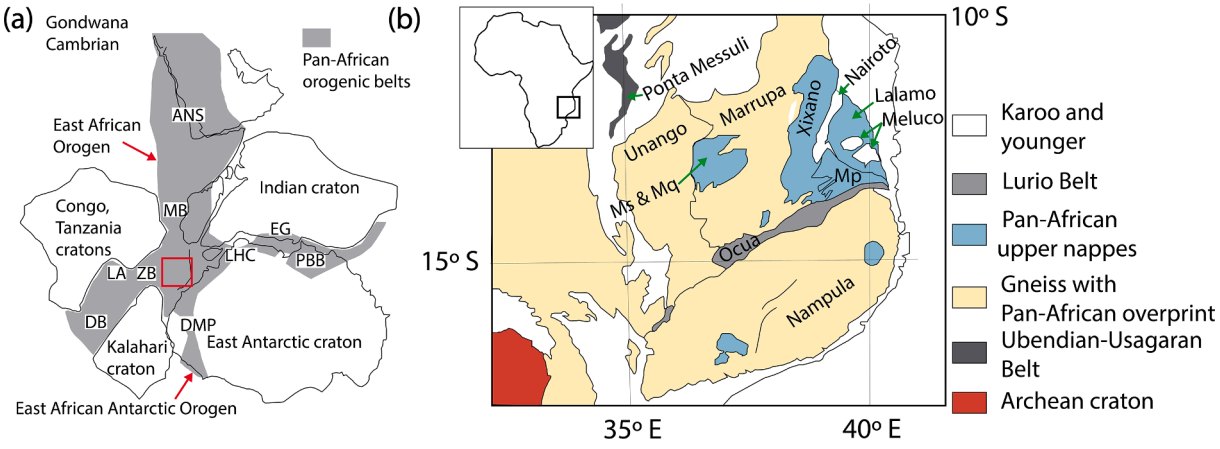

Fig. 1. (a) Cambrian reconstruction of Gondwana, with the location of the NE Mozambique (after Meert, 2003). (b) Simplified geological map of Northeastern Mozambique (adapted from Engvik et al., 2019). Highlighted are the main megatectonic units in the region. Abbreviation: ANS = Arabian–Nubian Shield, DB = Damara Belt; DMP = Dronning Maud Province; EG = Eastern Ghats; LA = Lufilian Arc; LHC = Lützow–Holm Complex; MB = Mozambique Belt; Ms = M'Sawize; Mp = Montepuez; Mq = Muaquia; PBB = Prydz Bay Belt and ZB = Zambezi Belt. The East-African Antarctic orogen (EAAO) includes the ANS, MB and DMP.

et al., 2010; Grantham et al., 2011). (5) The last megatectonic unit is interpreted as a tectonic mélange formed by slices of the adjoining complexes, which were deformed, transposed and dismembered during the Pan-African tectonic evolution (Engvik et al., 2007). It is made of the Neoproterozoic Montepuez and Ocua Complexes, with the latter forming the core of the Lurio Belt (Viola et al., 2008). A simplified geological map of Northeastern Mozambique is shown in Fig. 1b.

The Mazua ultramafic intrusion lies in the Nampula Complex, also known as the Nampula Block, which is the largest crustal Mesoproterozoic block in Northeastern Mozambique, covering approximately 100,000 km^2, formed during the widespread ~1 Ga mountain-building episode but with an intense Neoproterozoic-Cambrian overprint, due to the formation of the EAO and the supercontinent Gondwana (Macey et al., 2010). A simplified geological map of the Nampula Block is given in Fig. 2. The oldest lithodemic units of the Nampula Block include (1) the Suite of Mocuba, characterized by a metavolcanic-plutonic rock assemblage, (2) the Rapale Orthogneisses and (3) a sequence of supracrustal paragneisses and metavolcanic rock assemblage, known as the Molocue Group (Macey et al., 2010). These supracrustal rocks and granitoids were intruded by granitic orthogneisses of the Culicui Suite (Norconsult Consortium, 2007; Macey et al., 2010). The rest of the block consists of two overlying units of metasedimentary gneisses, the Mecubúri and Alto Benfica Groups (Norconsult Consortium, 2007; Thomas et al., 2010). The block was also intruded by many granitoid plutons and dikes of the Murrupula Suite and the Malema Suite during Cambro-Ordovician (Norconsult Consortium, 2007; Macey et al., 2010).

2.2. Geology of the Mazua ultramafic intrusion and related oxide ores

Fig. 3 shows a geological map of the Mazua area, on which the sample localities and trenches are highlighted. The Mazua ultramafic intrusion is a 10 km long body that hosts Fe-Ti oxide ores, ranging in confirmed thickness from 6 to 20 m (Geological Institute Belgrade, 1984; Cílek, 1989; Norconsult Consortium, 2007). The Mazua ultramafic intrusion is characterized by fine- to medium-grained hornblende pyroxenite and rarely crops out on the surface. The orebody is found under a quite thick layer of laterite of about 2 m (Geological Institute Belgrade, 1984). The exposed parts of the intrusion are coated by hydroxide minerals such as goethite (Fig. 4a-b). The ore-bearing rock is composed mainly of pyroxene, amphibole and Fe-Ti oxides, mostly ilmenite. The age of the Mazua ultramafic intrusion is still unknown; it might be related to several mafic dikes in the Nampula Block that were assumed

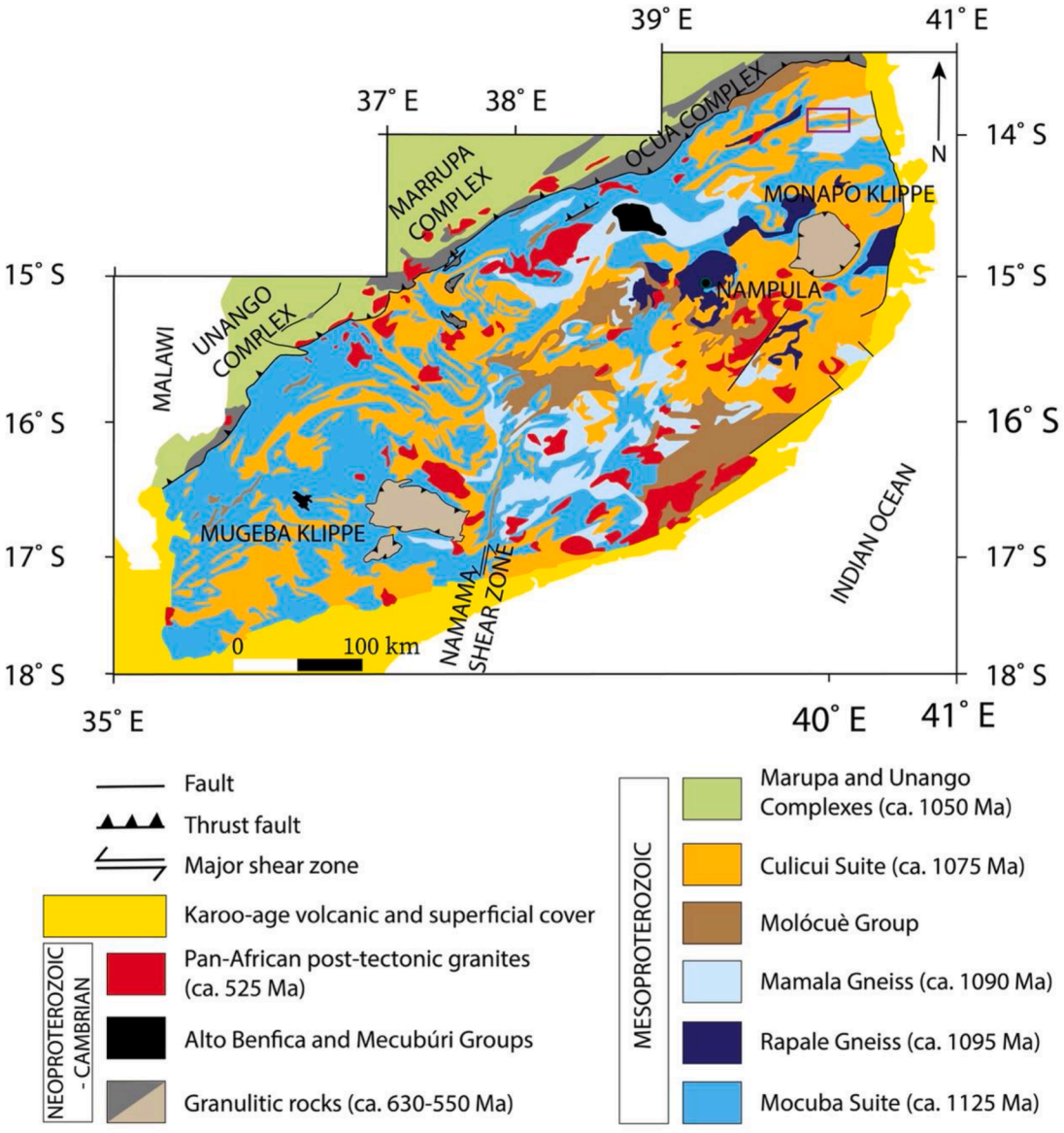

Fig. 2. Simplified geological map of the Nampula Block (modified from Macey et al., 2010). The rectangle shows the location of the Mazua ultramafic intrusion.

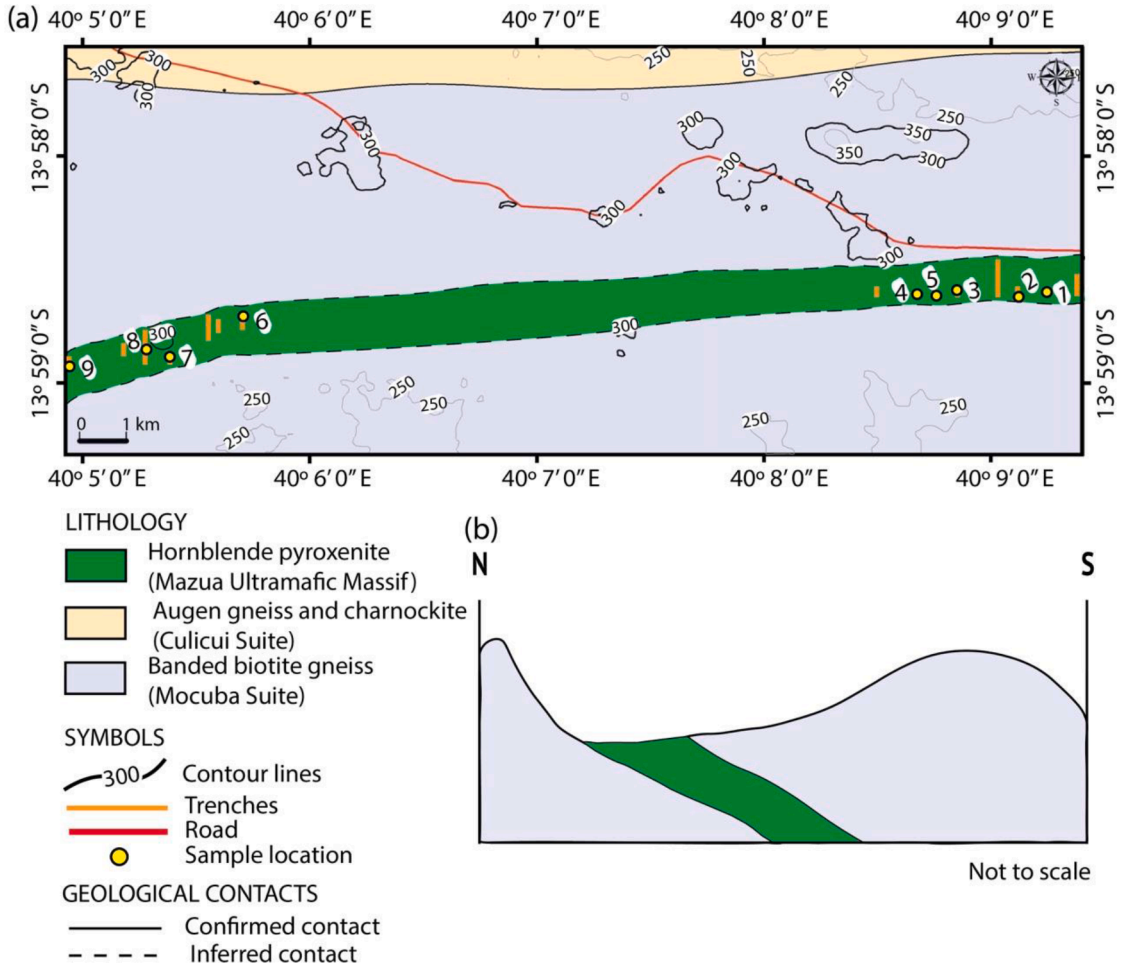

Fig. 3. (a) Geology of the Mazua area (adapted from Norconsult Consortium, 2007). (b) Schematic section showing a sharp contact between hornblende pyroxenite and banded biotite gneiss (adapted from Mandlaze, 2013). Sample location: 1 = Mzo1-st (oxide ore sample); 2 = Mzo15-ho (silicate-rich sample); 3 = Mzo4-lo/ho (oxide ore and silicate-rich samples); 4 = Mzo16-ho (oxide ore sample); 5 = Mzo17-ho (oxide ore sample); 6 = Mzo9-ho (silicate-rich sample); 7 = Mzo8-ho (silicate-rich sample); 8 = Mzo7-ho/mo (oxide ore samples) and 9 = Mzt10-ho (silicate-rich sample). Samples 1–5 are interpreted to be close to the bottom contact, while samples 6–9 are close to the top of the intrusion. The interval of contour lines is 50 m.

by Macey et al. (2010) to have formed in the Late Mesoproterozoic.

The country rocks at Mazua are characterized by Mesoproterozoic banded biotite gneiss belonging to the Mocuba Suite and augen gneiss and migmatite of the Culicui Suite (Norconsult Consortium, 2007). In some areas, the gneissic rocks are partly covered by lateritic materials that are composed of poorly sorted quartz grains cemented by iron hydroxides (Fig. 4c). Some garnet-bearing amphibolite enclaves with oval shapes occur randomly as small lenses in the intrusive rocks (Fig. 4d). The characteristics of the country rocks were described by Mandlaze (2013) and Unganai (2019).

Although field relationships are poorly understood due to the poor exposure of the Mazua ultramafic intrusion and the fact that no drilling program has been carried out, the intrusion seems to occur as interfoliave dyke-like intrusion. It progresses along the foliation by numerous finger-like penetrations (Geological Institute Belgrade, 1984). Mafic dykes intruding parallel to the dominant structural fabric of the country rocks in the Finlayson Lake greenstone belt, Canada were reported by Backeberg (2015). The banded biotite gneiss, which is the main country rock in the Mazua area, occurs in sharp contact with the ore-bearing rocks. The contact between these rocks is concordant to the regional E-W trend of the Nampula Block and gently dips northward at 45° (Fig. 3b).

2.3. Modes of occurrence of Fe-Ti oxides

The Fe-Ti oxide ores crop out in two different parts of the Mazua ultramafic intrusion (Fig. 3). They occur as veins, lenses and layers, either massive or disseminated in a fine- to medium-grained hornblende pyroxenite (Fig. 5). Fe-Ti oxides are disseminated in the oxide hornblende pyroxenite, whereas Fe-Ti oxide ores are characterized by millimeter to centimeter-scale Fe-Ti oxide layers and massive oxides (see the rock classification criteria in the next section). The contacts between oxides ores and adjacent silicate rocks are very sharp. Centimeter-scale size-graded silicate-rich layers are common in Mazua as shown in Fig. 5a and Fig. A.1 in the Electronic Supplementary Material (ESM 1).

2.4. Deformation and metamorphism

The Nampula Block experienced several phases of deformation (Macey et al., 2010; Grantham et al., 2011). D_1 deformation during the amphibolite facies metamorphism was recorded in the Mocuba Suite gneisses and characterizes intrafolial folds and refolded leucosomes (Grantham et al., 2011). A major phase of penetrative regional D_2 deformation was associated with the Pan-African event that completely affected the Nampula Block (Grantham et al., 2011). In addition to the upper amphibolite facies assemblages that characterized the Nampula Block, granulite facies conditions are locally recognized by the

Fig. 4. (a-b) Fine-grained ilmenite-bearing pyroxenite coated by Fe-Ti hydroxides such as goethite due to weathering. (c) Lateritic material covering the biotite gneiss consisting of inequigranular quartz clasts cemented by iron hydroxides. (d) Weathered garnetiferous amphibolite with foliation striking E-W and dipping northward at a moderate angle.

occurrences of metamorphic ortho- and clinopyroxenes in mafic gneisses and metapelites (Norconsult Consortium, 2007; Macey et al., 2010; Grantham et al., 2011). In Mazua such facies are recorded in the country rocks and are well described by Mandlaze (2013). Deformation overprints are less expressed in the Mazua ultramafic intrusion. Some primary magmatic textures are still preserved, and the ore-bearing rocks are less foliated suggesting a weak to non-pervasive deformation overprint (Fig. 5). Re-equilibration textures of Fe-Ti oxides and replacement of pyroxenes by secondary amphiboles and Fe-Ti oxides may represent metamorphic products. Barnes et al. (2016) reported similar textures in the study of pyroxene textures and their implications for crystallization mechanisms in the Ntaka Ultramafic Complex, Tanzania. They suggested that the less pervasive hydration and lesser development of tectonic fabric within the ultramafic rocks resulted from a strong partitioning of strain (Barnes et al., 2016). Such an interpretation can be applied to the Mazua ultramafic intrusion.

3. Analytical methods

3.1. Whole-rock chemistry

Concentrations of major and minor element oxides were determined using a Rigaku ZSX Primus II X-ray fluorescence spectrometer (XRF) at Akita University, Japan. Since the rocks from the Mazua ultramafic intrusion are rich in Fe-Ti (Norconsult Consortium, 2007), the Geological Survey of Japan (GSJ) geochemical reference samples which include the JP-1 peridotite and JGb-1 gabbro (Imai et al., 1995) were mixed with chemical reagents of Fe_3O_4 and TiO_2 powders and a Chemplex Industries SpectroBlend 44 μ Powder binder (CH660: $C_{19}H_{38}ON$) to ensure the reliability of analysis (Table B.1; ESM 2). The mixture was homogenized with an agate mortar for approximately 40 min. The samples were dried in the oven overnight at 110 °C and finally pressed powder pellets were prepared for analysis. The measurement conditions are given in Table B.2 (ESM 2). The FeO concentration in the rocks was determined by titration using $KMnO_4$ solution (Table B.3; ESM 2). The Fe_2O_3 concentration was therefore calculated stoichiometrically from the $Fe_2O_{3\_Total}$ determined by XRF (Table 1).

Powdered samples were analyzed by ALS Geochemistry, North Vancouver, Canada, for whole-rock concentrations of trace elements [rare-earth elements (REE), Li, Be, V, Co, Ni, Cu, Zn, Ga, Ge, As, Se, Rb, Sr, Y, Zr, Nb, Mo, Ag, Cd, In, Sn, Sb, Te, Cs, Ba, Hf and Ta]. In a Zr crucible, 0.2 g of each powdered samples was fused with a sodium peroxide flux (Na_2O_2) at 670 °C. The fused mixture was later dissolved in 30 % hydrochloric acid (HCl) and the resulting solution was analyzed by an inductively coupled plasma mass spectrometer (ICP-MS).

Powdered samples with 0.1 g weight were digested by solutions of perchloric acid ($HClO_4$), hydrofluoric acid (HF), and nitric acid (HNO_3), for the determination of Zr, Hf, Cr and Sc concentrations using an Agilent 7500 Series ICP-MS at Akita University. The JA-2 andesite from the GSJ (Imai et al., 1995) was used as standard material to check the reliability of the analysis.

In addition to the usual major and trace elements determined by XRF, the loss on ignition (LOI) was measured at 900 °C. The LOI values at Mazua record a weight gain caused by oxidation of the samples during the heating process, mainly due to their Fe-rich nature (Table 1).

3.2. Mineral chemistry

The compositions of pyroxene were determined using a JEOL JXA-8800 wavelength-dispersive spectrometry electron probe microanalyzer (EPMA) at Akita University. The analyses were performed using an accelerating voltage of 15 kV and a beam current of 15nA. Peak

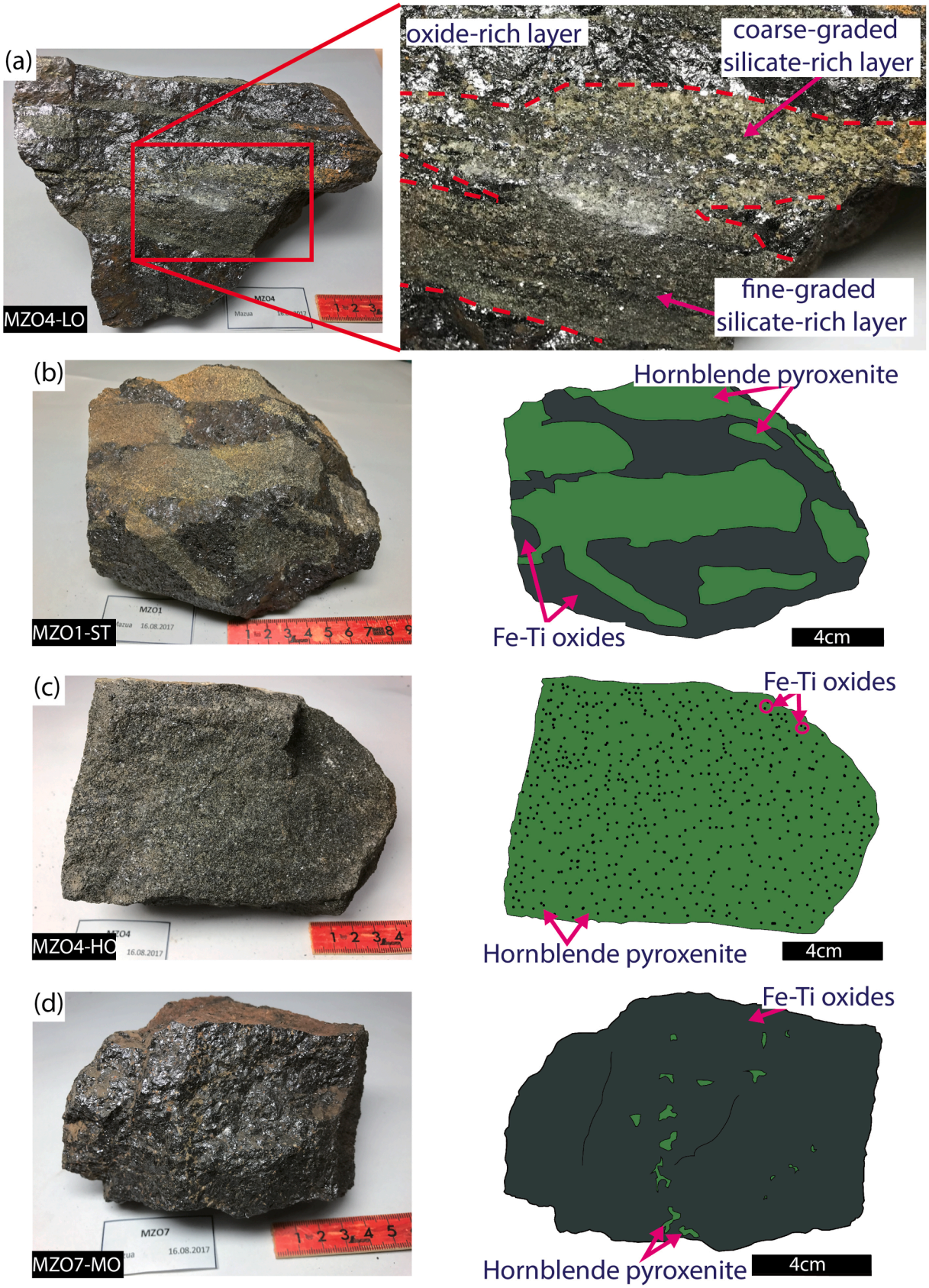

Fig. 5. Modes of occurrence of Fe-Ti oxide ores in Mazua. (a) Layered, (b) vein-like, (c) disseminated, and (d) massive ores. The layered Fe-Ti oxide ore shows a centimeter-scale graded silicate-rich interlayer. The sample location is shown in Fig. 3.

Table 1
Major and trace element compositions of oxide hornblende pyroxenite and Fe-Ti oxide ores of the Mazua ultramafic intrusion.

Sample ID	Mzo1-st	Mzo4-ho	Mzo4-lo	Mzo7-ho	Mzo7-mo	Mzo8-ho	Mzo9-ho	Mzt10-ho	Mzo15-ho	Mzo16-ho	Mzo17-ho
Rock	FTO	OHP	FTO	FTO	FTO	OHP	OHP	OHP	OHP	FTO	FTO
Major and minor elements (wt. %)											
SiO_2	32.11	41.33	42.88	34.49	2.88	31.58	42.13	48.42	47.96	24.73	20.99
TiO_2	21.97	10.89	11.97	18.32	43.08	20.89	2.51	5.83	6.62	27.07	29.12
Al_2O_3	1.70	1.20	1.42	1.39	2.53	2.22	6.51	1.44	1.32	1.96	2.03
Fe_2O_3	7.68	7.98	5.69	4.16	12.46	6.42	10.91	7.29	4.71	4.68	5.71
FeO	22.63	16.11	16.41	21.14	36.28	23.65	16.77	13.17	14.85	28.14	30.06
MnO	0.21	0.22	0.22	0.25	0.31	0.29	0.29	0.30	0.22	0.25	0.24
MgO	8.22	10.72	10.18	9.03	3.26	7.27	12.73	11.76	10.62	7.89	8.18
CaO	5.85	11.85	11.25	9.53	0.09	7.80	7.97	11.81	13.63	5.36	3.75
Na_2O	0.12	0.27	0.17	0.24	0.11	0.25	0.82	0.31	0.21	0.17	0.18
K_2O	0.05	0.02	0.02	0.03	0.01	0.05	0.13	0.07	0.04	0.02	0.02
P_2O_5	0.00	0.01	0.10	1.59	0.00	0.00	0.02	0.04	0.04	0.00	0.06
LOI	−2.08	−1.14	−0.99	−1.54	−4.16	−2.04	−0.47	−0.47	−0.67	−2.88	−2.89
H_2O*	0.44	0.65	0.84	0.81	−0.12	0.59	1.40	1.00	0.98	0.25	0.46
Total†	101.0	101.3	101.2	101.0	100.9	101.0	102.0	101.4	101.2	100.5	100.8
Mg#	0.34	0.46	0.47	0.41	0.11	0.32	0.47	0.53	0.51	0.31	0.30
Trace elements (ppm)											
Li	12	11	12	9.0	10	10	7.0	12	13	8.0	9.0
Be	<0.4	<0.4	<0.4	<0.4	<0.4	<0.4	<0.4	<0.4	<0.4	<0.4	<0.4
Sc	115	110	73.5	n.a.	111	109	76.5	100	123	107	n.a.
V	2450	1440	2430	1620	2600	766	1140	824	1040	2160	1760
Cr	1540	1120	962	n.a.	626	728	840	538	704	1160	n.a.
Co	170	114	151	203	156	98	128	90	99	160	133
Ni	270	260	220	330	180	190	250	180	250	230	280
Cu	<20	<20	<20	<20	<20	<20	<20	<20	<20	<20	<20
Zn	230	160	270	250	310	130	200	120	110	230	190
Ga	7.0	11	5.2	7.1	3.5	6.5	12	6.2	6.8	4.6	7.3
Ge	0.7	2.2	0.8	1.6	0.5	2.4	1.3	2.0	2.5	1.0	1.3
As	9.0	19	8	58	70	10	6.0	11	39	11	4
Se	5.0	<3	6.0	<3	12	6.0	8.0	6.0	6.0	4.0	15
Rb	2.6	1.6	1.2	1.3	1.0	0.7	1.1	0.8	1.4	0.8	0.9
Sr	<20	<20	<20	30	<20	<20	50	<20	<20	<20	<20
Y	16	37	20	101	10	33	29	34	42	26	42
Zr	30	27	14	n.a.	12	24	50	20	24	21	n.a.
Nb	27	15	40	24	52	4.1	8.9	4.7	6.8	38	22
Mo	2.0	2.0	3.0	<2	<2	<2	<2	<2	<2	2.00	<2
Ag	<5	10	6.0	6.0	10	8.0	<5	<5	<5	<5	<5
Cd	<0.8	0.9	<0.8	<0.8	<0.8	<0.8	<0.8	<0.8	<0.8	<0.8	<0.8
In	<0.3	<0.3	<0.3	<0.3	<0.3	<0.3	<0.3	<0.3	<0.3	<0.3	<0.3
Sn	<3	<3	<3	<3	<3	<3	<3	<3	<3	<3	<3
Sb	3.0	1.7	3.9	4.8	0.8	1.7	2.4	0.6	4.5	3.0	2.0
Te	0.5	<0.5	0.7	0.5	0.9	0.7	0.5	<0.5	<0.5	0.6	<0.5
Cs	0.2	0.3	1.6	0.1	0.1	0.1	2.9	0.1	0.2	<0.1	0.1
Ba	17	52	32	100	21	89	17	51	50	21	27
La	2.0	1.7	3.1	16	3.0	5.3	3.7	5.3	3. 9	7.1	7.1
Ce	2.9	4.7	7.9	21	3.4	12	6.3	10	6.7	3.8	8.7
Pr	0.83	1.3	1.6	6.2	1.4	2.3	1.7	2.4	2.2	2.0	2.8
Nd	4.9	9.5	9.1	37	7.2	14	11	14	13	11	16
Sm	1.9	4.0	3.0	10	1.5	5.1	4.2	5.5	5.3	2.7	5.4
Eu	0.42	0.8	0.53	2.2	0.38	1.1	0.97	0.96	1.1	0.69	0.99
Gd	2.4	5.9	4.5	15	2.1	6.1	5.5	5.9	7.3	3.9	6.9
Tb	0.38	0.95	0.61	2.2	0.29	1.0	0.84	0.94	1.1	0.53	1.0
Dy	2.7	6.9	4.4	13.8	1.9	6.4	5.3	6.2	7.6	3.9	7.7
Ho	0.52	1.4	0.77	3.0	0.37	1.3	1.1	1.3	1.5	0.79	1.5
Er	1.4	4.2	2.5	8.9	1.1	3.7	2.8	3.6	4.1	2.5	4.5
Tm	0.21	0.54	0.37	1.1	0.15	0.55	0.41	0.49	0.57	0.32	0.77
Yb	1.8	3.6	2.5	7.4	1.2	3.2	2.1	3.4	3.8	2.5	4.8
Lu	0.3	0.54	0.48	1.3	0.24	0.42	0.39	0.51	0.52	0.34	0.79
Hf	1.7	1.4	0.96	n.d.	0.77	1.3	1.9	1.1	1.2	1.3	n.d.
Ta	2.4	1.4	3.0	1.9	3.8	0.36	0.65	0.25	0.43	5.5	1.8
Th	0.1	0.1	0.2	0.2	0.1	0.4	0.1	0.3	0.1	0.2	0.1
U	0.3	0.5	0.5	0.5	0.3	0.5	0.3	0.4	0.5	0.4	0.3

*H_2O calculated from LOI and FeO
†The LOI is not included in the total of major elements
Mg# = [MgO/(MgO + FeO_{Total}), molar]
Abbreviation: OHP = oxide hornblende pyroxenite, FTO = Fe-Ti oxide ore and n.a. = not analyzed

and background counting times were 20 s and 10 s, respectively. The concentration of elements was determined using analyzing crystals of LIF (lithium fluoride, LiF) for Fe Kα, Mn Kα and Cr Kα; PET (pentaerythritol, $C_5H_{12}O_4$) for Ca Kα, Ti Kα and K Kα and TAP (thallium acid phthalate, $C_8H_5O_4Tl$) for Al Kα, Na Kα, Si Kα and Mg Kα. Reference standards used include wollastonite for Si and Ca, TiO_2 for Ti, kyanite for Al, hematite for Fe, MnO for Mn, periclase for Mg, albite for Na, K-feldspar for K and eskolaite for Cr. The oxide-ZAF correction was applied for quantitative analysis. The ferrous and ferric iron concentrations were estimated from stoichiometry and charge balance following the method

of Droop (1987).

The compositions of the Fe-Ti oxides in the samples from Mazua were determined using the same JEOL JXA-8800 EPMA, at Akita University, under the following analytical conditions. A beam current of 10 nA and an acceleration voltage of 15 kV. The analyzing crystals were LIF for Fe Kα, Mn Kα, Cr Kα and Ni Kα, PET for Ti Kα and V Kα and TAP for Al Kα, Si Kα and Mg Kα. Natural and synthetic standards were used for calibration, TiO_2 for Ti, kyanite for Al, eskolaite for Cr, V (pure metal) for V, hematite for Fe, NiO for Ni, MnO for Mn, periclase for Mg and wollastonite for Si. The oxide-ZAF correction was also applied for quantitative analysis of Fe-Ti oxides.

The overlap of the $K\beta_{1,3}$ X-ray emission line of Ti ($\lambda = 2.514$ Å) with the $K\alpha_{1,2}$ line ($\lambda = 2.505$ Å) of V was corrected in the JEOL EPMA software using a coefficient of 0.10796. The peak and background counting times were 20 s and 10 s, respectively for all the elements, with the exception of V and Ti. For Ti and V, the peak and background counting times of 50 s and 25 s were chosen. It was not possible to analyze separately the hematite that resulted from the oxidation of magnetite because of its size less than ca. 2 μm. Ferrous and ferric iron concentrations of Fe-Ti oxides were estimated from stoichiometry and charge balance following the method of Carmichael (1967). Detection limit information for quantitative analyses by EPMA is given in Table B.4 (ESM 2).

4. Petrography

The two-fold lithological classification was adopted for the rocks from the Mazua ultramafic intrusion, following the same concept of Bai et al. (2012). Thus, the samples composed of < 50 vol% of Fe-Ti oxides were referred to as oxide hornblende pyroxenite, whereas the samples

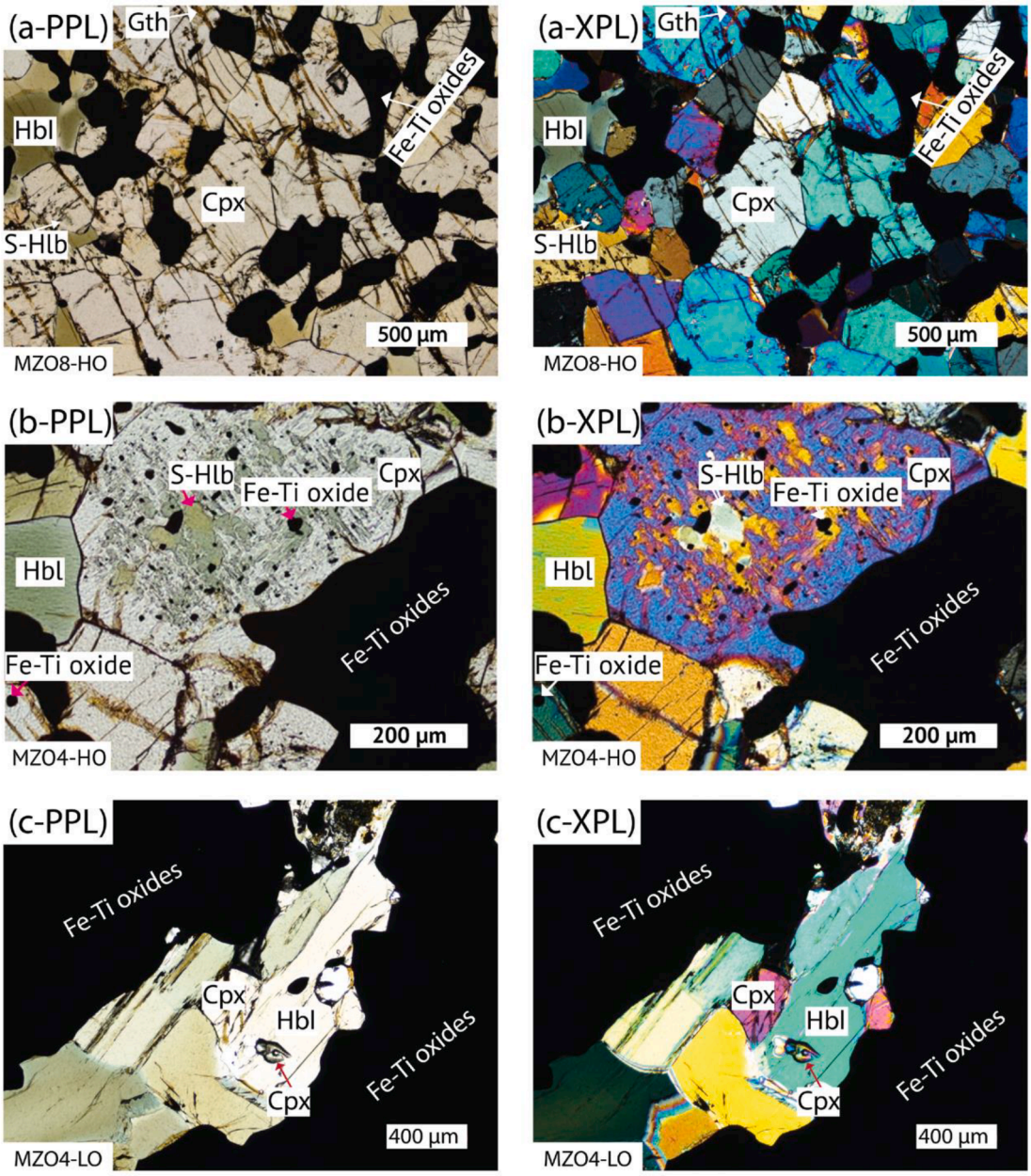

Fig. 6. Photomicrographs (PPL - plane polarized transmitted light and XPL - crossed polarized transmitted light) from Mazua. (a) Massive equigranular hornblende pyroxenite with interstitial Fe-Ti oxides. (b) Replacement of clinopyroxene by secondary amphibole and Fe-Ti oxides. Note the 120° interfacial angles formed at three-grain junctions. (c) Prismatic silicate minerals showing a layering texture in a Fe-Ti oxide ore sample. Abbreviation: Cpx = clinopyroxene; Hbl = hornblende; S-Hbl = secondary hornblende; Gth = goethite

with > 50 vol% of Fe-Ti oxides were classified as Fe-Ti oxide ores (see representative samples in Table C.1; ESM 3).

4.1. Oxide hornblende pyroxenite

Oxide hornblende pyroxenite shows massive equigranular texture and is mainly composed of clinopyroxene, amphibole, Fe-Ti oxides and very minor amounts of orthopyroxene, apatite and olivine (Fig. 6a). Straight to curved boundaries between minerals are very common in all the samples. Locally, boundaries between adjacent clinopyroxene and amphibole appear serrated, suggesting local re-equilibration. Clinopyroxene is euhedral to subhedral (<500 μm in length) and partly replaced by blebs of secondary amphibole and associated secondary Fe-Ti oxides (Fig. 6b). This replacement process might have been either related to the exsolution of clinopyroxene, or may have resulted from hydration processes caused during metamorphism (e.g. Buseck et al., 1980; Gillis and Meyer, 2001). The blebs of amphibole are pale green and are preferentially oriented. The size of the blebs is smaller than 100 μm and the associated Fe-Ti oxides are even smaller (<50 μm). The magmatic amphibole is brownish-green in color and mostly occurs as an interstitial filling between the early crystallized pyroxenes and Fe-Ti oxides (Fig. A.1; ESM 1). Orthopyroxene occurs in only one sample (Mzo9-ho). It shows euhedral habit and is larger than clinopyroxene (>500 μm). Replacement texture of silicate minerals by botryoidal goethite due to

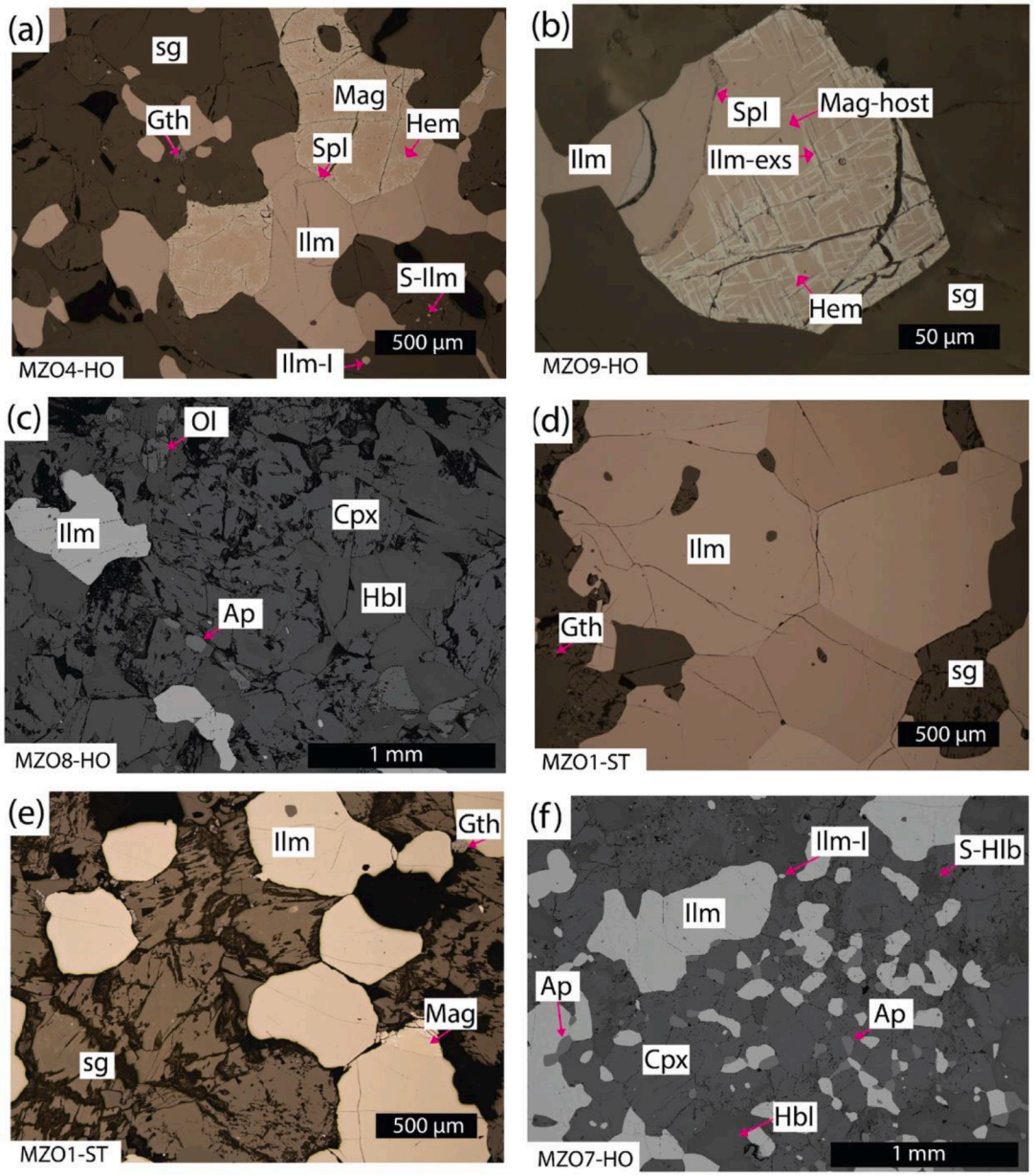

Fig. 7. Reflected light photomicrographs and backscattered-electron (BSE) images of the oxide hornblende pyroxenite (a-c) and Fe-Ti oxide ore (d-f) from the Mazua ultramafic intrusion. (a) Interstitial fillings of ilmenite and magnetite with annealing textures. Note the occurrence of hematite in magnetite, secondary ilmenite associated with amphibole blebs. (b) Ilmenite exsolution lamellae in a magnetite host. Secondary hematite occurs in magnetite along fractured areas. Very thin Al-rich spinel is distributed at the boundary between ilmenite and magnetite. (c) BSE image showing interstitial minor apatite grains between silicates. Note the minor occurrence of small fractured olivine grains. (d) Monomineralic aggregates of ilmenite with annealing textures. (e) Chained ilmenite grains in contact with small magnetite. (f) BSE image showing interstitial ilmenite and apatite between monomineralic ilmenite lenses. Mineral abbreviation: Cpx = clinopyroxene; Ol = olivine; Hbl = hornblende; S-Hbl = secondary hornblende; Ilm = ilmenite; Mag = magnetite; Hem = hematite; Spl = spinel; Gth = goethite; Ilm-I = ilmenite inclusion; S-Ilm = secondary ilmenite; and Ilm-exs = exsolved ilmenite; Ap = apatite and sg = silicate gangue

supergene processes is very common in all the samples.

Fe-Ti oxides occur as anhedral to subhedral and locally globular interstitial grains between silicate minerals and as some monomineralic aggregates of ilmenite (>2 mm) surrounding silicate minerals (Fig. 7a). In some samples, magnetite is almost absent. Small inclusions of ilmenite are present in amphibole and clinopyroxene. Boundaries between the Fe-Ti oxides and silicates are straight to slightly curved. The interfacial angles between the ilmenite grains in monomineralic aggregates are approximately 120°, displaying characteristic subsolidus annealing textures (Fig. 7a). Besides its occurrence as an early crystallized phase along with magnetite and as an exsolved phase in magnetite, ilmenite also appears to be associated with secondary hornblende resulted from the replacement of clinopyroxene. Its size and habit are similar to the primary ilmenite inclusions in silicate minerals (Fig. 7a). Hematite occurs as very thin lamellae along the fractures resulted from the oxidation of magnetite (Fig. 7b). Secondary arsenopyrite characteristically occurs along the ilmenite boundaries. Very small and minor apatite grains occur in interstices between clinopyroxenes (Fig. 7c).

4.2. Fe-Ti oxide ores

Fe-Ti oxide ores are characterized by alternating layers or banding of silicates and Fe-Ti oxides. Thickness of the layers varies significantly from millimeters to centimeters. The thinner layers are characterized by elongated and prismatic minerals such as clinopyroxene and primary amphibole and the boundaries between them are straight and do not show any reaction textures. The prismatic habit of primary amphibole, which occurs along with clinopyroxene, is consistent with its magmatic origin (Fig. 6c). On the other hand, the thick layers consist chiefly of clinopyroxene with subhedral to euhedral habit, hornblende and Fe-Ti

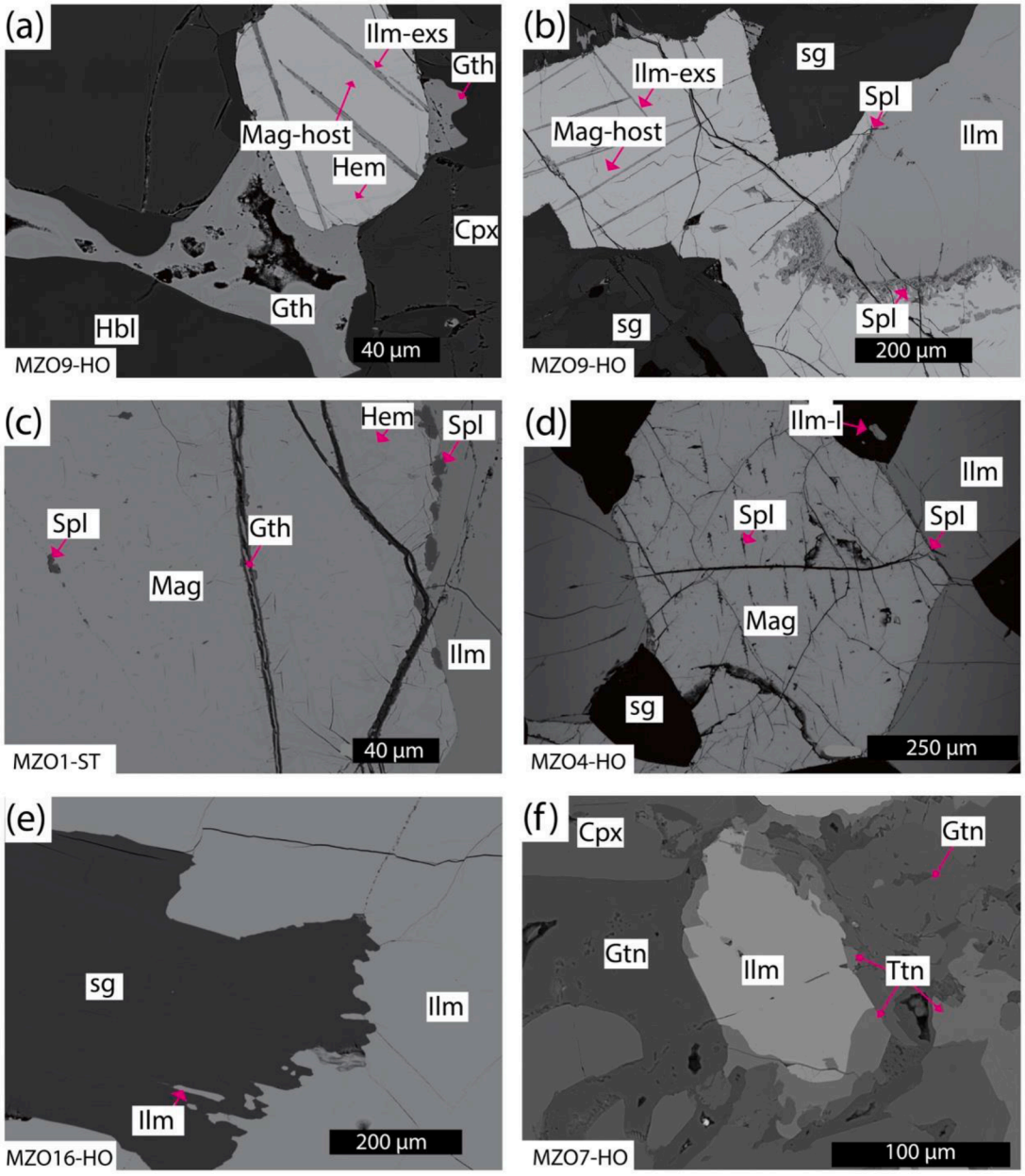

Fig. 8. Back-scattered electron (BSE) images showing different types of micro-intergrowths in the Fe-Ti oxides. (a-b) Cloth-like lamellae of exsolved ilmenite in magnetite. (c-d) Reaction rims of Al spinel at Fe-Ti oxides contact. Fine pattern exsolution lamellae (trellis) and blebs of Al-spinel in magnetite are noteworthy. (e) Silicate-oxide re-equilibration textures. (f) Ilmenite partially replaced and rimmed by titanite. Mineral abbreviation: Ttn = titanite. See Fig. 7 for other mineral abbreviation.

oxides. Textural characteristics of these minerals are very similar to those of oxide hornblende pyroxenite.

Fe-Ti oxides ores are mainly composed of layers of large monomineralic aggregates of ilmenite (0.05 – 2.5 mm) and chained euhedral ilmenite grains (Fig. 7d-e). These layers form straight contacts with thin silicate layers. Within the layers, some oxides occur as interstitial fillings and their size is<1 mm. The boundaries between the grains in the monomineralic aggregates are straight and subsolidus annealing textures are common (Fig. 7d). As in the oxide hornblende pyroxenite, secondary fine ilmenite grains associated with amphibole blebs are common. Magnetite occurs in trace amounts and contains lamellae of hematite (Fig. 7e). Zircon occurs in trace amounts as inclusions in ilmenite of monomineralic aggregates. Significant amounts of apatite occur in interstices between monomineralic ilmenite layers in sample Mzo7-ho (Fig. 7f).

4.3. Microtextures of oxides

Different types of micro-intergrowths of Fe-Ti oxides are observed in the Fe-Ti oxide ores and the oxide hornblende pyroxenite from the Mazua ultramafic intrusion. They include (1) cloth-like lamellae of ilmenite hosted in magnetite (Fig. 8a-b), (2) fine pattern exsolution trellis lamellae and blebs of aluminous spinel in magnetite (Fig. 8c-d), (3) discontinuous rims of aluminous spinel distributed at the boundary between magnetite and ilmenite in both rock types (Fig. 8b-d), (4) reaction texture involving Fe-Ti oxides and Fe-Mg silicates (Fig. 8e) and (5) partial replacement of ilmenite by secondary titanite (Fig. 8f).

5. Whole-rock geochemistry

5.1. Major and minor elements

The bulk major element composition of the rocks of the Mazua

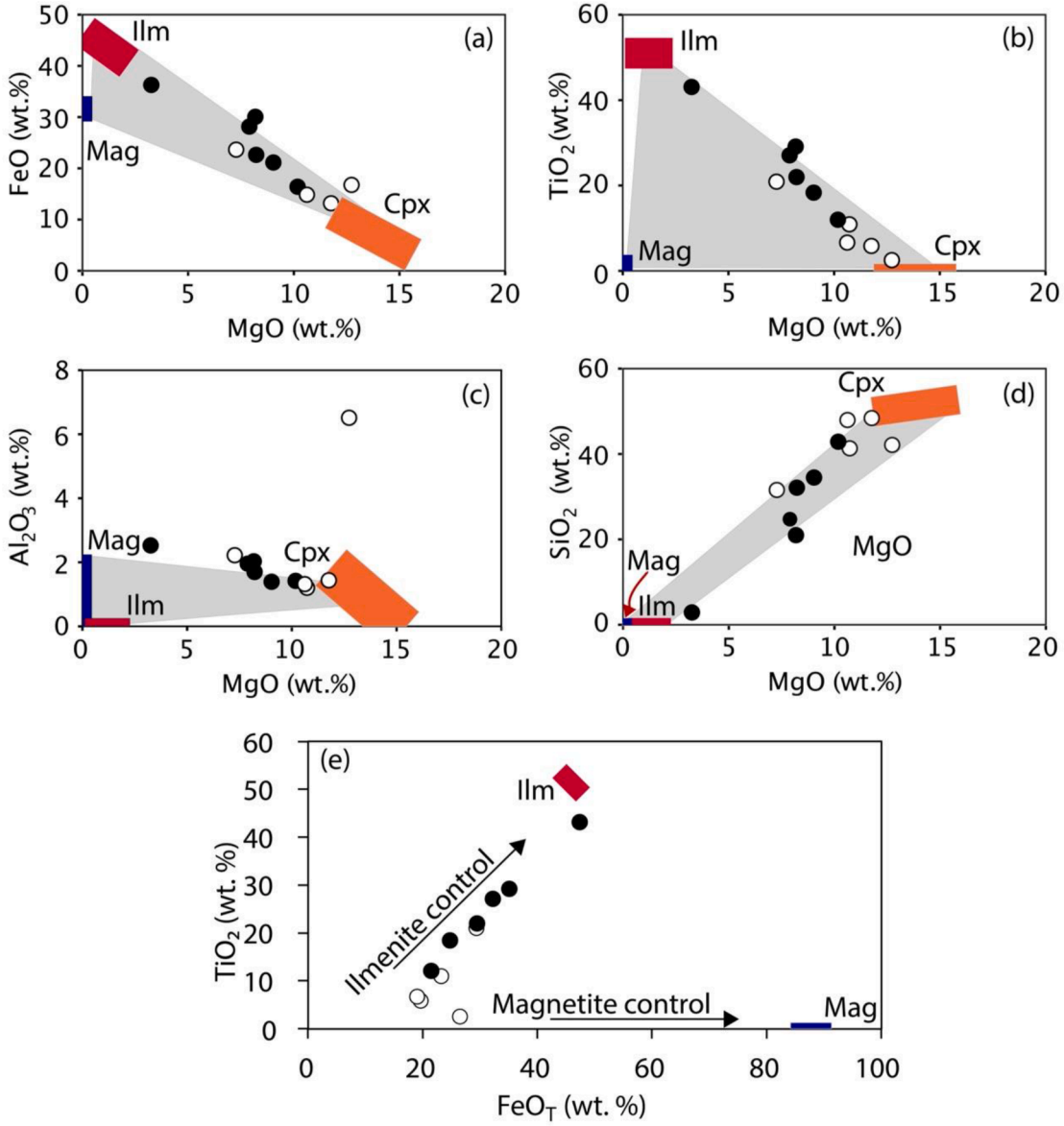

Fig. 9. Variations of whole-rock FeO (a), TiO_2 (b), Al_2O_3 (c) and SiO_2 (d) with MgO in the oxide hornblende pyroxenite and Fe-Ti oxide ores from the Mazua ultramafic intrusion. (e) Bivariate diagram of whole-rock TiO_2 vs. FeO_{Total} of Fe-Ti oxide ores and oxide hornblende pyroxenite. The compositional ranges of the minerals, determined in the present study by EPMA, are represented by colored boxes. The gray boxes represent the trajectories of the plotted minerals space. The open and filled circles stand for oxide hornblende pyroxenite and Fe-Ti oxide ores, respectively. Mineral abbreviation: Mag = magnetite; Ilm = ilmenite, Hbl = hornblende and Cpx = clinopyroxene.

ultramafic intrusion is variable (Table 1). In general, the concentrations of FeO and TiO_2 of Fe-Ti oxide ores are higher, ranging from 16 to 36 wt % and 12 to 43 wt% respectively, compared to those of the oxide hornblende pyroxenite, ranging from 13 to 24 wt% and 3 to 21 wt%, respectively.

Binary plots demonstrate that the concentrations of major elements are mainly controlled by the modal abundance of clinopyroxene and Fe-Ti oxides including ilmenite and magnetite in the samples (Fig. 9a-d). Many samples fall outside of the trajectory of the plotted minerals in the SiO_2 and Al_2O_3 versus MgO diagrams most probably because of the presence of other Al – Si-rich phases such as amphibole (Fig. 9c-d). The influence of magnetite is insignificant in the rocks of the Mazua intrusion, with the exception of Mzo9-ho (an oxide hornblende pyroxenite, Fig. 9e) due to its abundance in such a rock. The variations of P_2O_5, Na_2O, and K_2O, all present at extremely low abundance, are independent from the rock types (Table 1). The true variations of Na_2O and K_2O might have been shadowed by weathering processes.

5.2. Trace elements

The trace element concentrations of the Mazua ultramafic intrusion are reported in Table 1. The concentrations of V vary from 1620 to 2600 ppm in Fe-Ti oxide ores, while those of the oxide hornblende pyroxenite are relatively low and vary from 766 to 1440 ppm. The Cr concentrations of the oxide hornblende pyroxenite vary from 538 to 1120 ppm, while those of the Fe-Ti oxide ores vary from 626 to 1540 ppm. The Co concentrations vary narrowly from 133 to 203 ppm and 90 to 128 ppm in the Fe-Ti oxide ores and oxide hornblende pyroxenite, respectively. The high concentration of these elements in the Fe-Ti oxide ores is because they are preferentially partitioned in Fe-Ti oxides. The Ni concentrations vary from 180 to 330 ppm in Fe-Ti oxide ores and from 180 to 260 ppm in oxide hornblende pyroxenite. Furthermore, the Zr concentrations of the oxide hornblende pyroxenite range from 20 to 50 ppm and those of the ores are very low.

Fig. 10 shows the primitive mantle-normalized alteration-resistant trace element patterns that are characterized by pronounced positive anomalies of Ta, Nb and Ti associated with negative anomalies of Zr and Hf. These geochemical fingerprints are more distinct in Fe-Ti oxide ores than in oxide hornblende pyroxenite.

6. Mineral chemistry

6.1. Silicates

The compositions of pyroxene in the Mazua ultramafic intrusion are given in Table 2. Average clinopyroxene composition ranges from Ca-rich augite to diopside (Wo_{44-49}, En_{36-41}, Fs_{11-21}) with Mg-numbers [defined as atomic 100 × Mg/(Mg + Fe^{2+} + Mn^{2+} + Fe^{3+})] varying from 64 to 79. No clear differences in clinopyroxene chemistry are found between the Fe-Ti oxide ores and oxide hornblende pyroxenite (Fig. A.2 in ESM 1). The TiO_2, Al_2O_3, and MnO concentrations are very weakly negatively correlated with the MgO concentrations in both the Fe-Ti oxides ores and oxide hornblende pyroxenite. Strong correlations of MgO concentrations with FeO (negative) and CaO (positive) concentrations are also noted in the Fe-Ti oxides ores and oxide hornblende pyroxenite. The Na_2O concentrations are not correlated with the MgO concentrations in the oxide hornblende pyroxenite, while a very weak correlation characterizes the Fe-Ti oxide ores (Fig. A.3 in ESM 1). Orthopyroxene is enstatite in composition (Wo_1, En_{53}, Fs_{46}) with a Mg-number of 53 in one sample (Mzo9-ho) of the oxide hornblende pyroxenite.

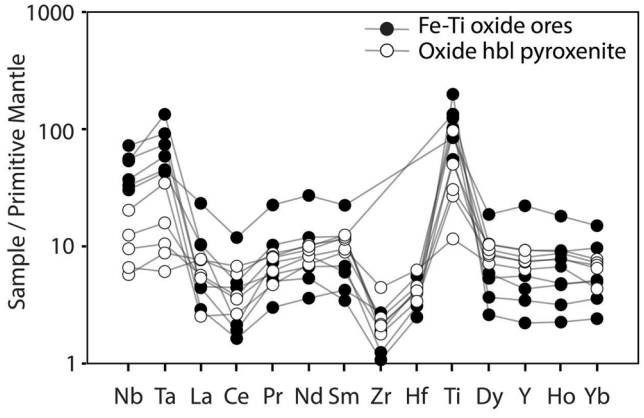

Fig. 10. Primitive mantle-normalized alteration-resistant trace element diagrams for Fe-Ti oxide ores and oxide hornblende from the Mazua ultramafic intrusion. Primitive mantle normalization values are from Sun and McDonough (1989). Hbl stands for hornblende.

6.2. Fe-Ti oxides

The composition of the primary ilmenite varies narrowly in the oxide hornblende pyroxenite and Fe-Ti oxide ores from the Mazua ultramafic intrusion (Table 3). It ranges from the $FeTiO_3$ end-member to 4 mol% hematite component. The MgO concentrations of primary ilmenite vary from 0.8 to 1.8 wt%, MnO from 0.4 to 0.5 wt%, Cr_2O_3 from below detection limit (b.d.l.) to 0.2 wt% and V_2O_3 from b.d.l. to 0.5 wt%. The TiO_2 and FeO concentrations of primary ilmenite in the oxide hornblende pyroxenite and Fe-Ti oxide ores are positively correlated while the V_2O_3 concentrations are negatively correlated with the TiO_2 concentrations (Fig. 11a-b). The MgO concentrations of primary ilmenite are not correlated with the TiO_2 in these rocks (Fig. 11c). The FeO and MgO concentrations in the Fe-Ti oxide ores are higher than those in the oxide hornblende pyroxenite (Fig. 11a and c). This compositional variation seems to be controlled by the relative proportion of clinopyroxene and Fe-Ti oxides in the ore-bearing rocks.

The compositions of ilmenite inclusions in silicate minerals are also reported in Table 3. They range from the $FeTiO_3$ end-member to 6 mol% hematite component. The TiO_2 concentrations of these inclusions vary from 49 to 52 wt%, FeO from 42 to 45 wt%, MgO from 0.8 to 1.9 wt% and V_2O_3 from b.d.l. to 0.5 wt%. The ilmenite inclusions show similar correlation patterns with those of the primary ilmenite (Fig. 11a-c). The MnO concentrations in all the rocks do not show any traceable correlation with the TiO_2 concentrations (Fig. 11d).

The secondary ilmenite is characterized by the TiO_2 concentrations that vary from 49 to 51 wt%, FeO from 42 to 45 wt% and MgO from 0.8 to 1.2 wt% (Table 3). The secondary ilmenite in sample mzo4-ho is compositionally similar to the ilmenite inclusions in sample mzo15-ho, where both are characterized by very low concentrations of TiO_2, MgO and FeO (Fig. 11). These low concentrations are compensated with very high Fe_2O_3 concentrations (5.6 to 6.3 wt%) when compared to the primary ilmenite and ilmenite inclusions in the same samples (Table 3).

The chemical composition of magnetite ranges from the end-member Fe_3O_4 to a titanomagnetite with 1 mol% ulvospinel component. The Al_2O_3 concentrations range from 0.3 to 0.5 wt%, Cr_2O_3 from 1.3 to 3.7 wt%, V_2O_3 from 1.7 to 2.7 wt% and MgO from 0.05 to 0.1 wt% (Table 4). The FeO concentrations are positively correlated with the TiO_2 concentrations, whereas the V_2O_3 and MgO concentrations are negatively correlated with the TiO_2 concentrations (Fig. 12a-c). The Al_2O_3 concentrations are not correlated with other elements in magnetite grains from Mazua (Fig. 12d).

7. Discussion

7.1. Subsolidus re-equilibration processes

The chemical composition of Fe-Ti oxides varies significantly in plutonic rocks mostly due to sub-solidus equilibration during cooling

Table 2
Compositions of clinopyroxene and orthopyroxene in the Fe-Ti oxide ores and oxide hornblende pyroxenite from the Mazua ultramafic intrusion.

Sample ID	Mzo1-st	Mzo4-ho	Mzo4-lo	Mzo7-ho	Mzo8-ho	Mzo9-ho	Mzt10-ho	Mzo15-ho	Mzo15-ho
Rock type	FTO	OHP	FTO	FTO	OHP	OHP	OHP	OHP	FTO
Mineral	Cpx	Cpx	Cpx	Cpx	Cpx	Opx	Cpx	Cpx	Cpx
N	8	34	7	15	8	15	28	6	8
Oxides (wt. %)									
SiO_2	51.27 (0.29)	52.87 (0.39)	52.08 (0.31)	52.98 (0.25)	49.37 (0.34)	51.28 (0.26)	52.82 (0.32)	51.20 (0.37)	53.11 (0.46)
TiO_2	0.09 (0.04)	0.08 (0.03)	0.06 (0.04)	0.10 (0.03)	0.15 (0.02)	0.07 (0.02)	0.11 (0.03)	0.07 (0.03)	0.08 (0.04)
Al_2O_3	0.64 (0.19)	0.56 (0.17)	0.55 (0.16)	0.82 (0.19)	1.56 (0.09)	1.11 (0.17)	0.82 (0.16)	0.57 (0.12)	0.56 (0.18)
Cr_2O_3	<0.10	0.12 (0.02)	<0.10	<0.10	0.12 (0.01)	<0.10	<0.10	<0.10	<0.10
Fe_2O_3	3.59 (0.60)	1.65 (0.73)	1.40 (0.41)	n.c.[a]	4.48 (0.75)	n.c.[a]	1.18 (0.52)	3.10 (0.71)	1.44 (0.37)
FeO	4.40 (0.68)	6.98 (0.84)	7.07 (0.47)	8.99 (0.51)	8.95 (0.81)	27.58 (0.31)	7.23 (0.55)	6.40 (0.34)	5.67 (1.14)
MnO	0.19 (0.06)	0.19 (0.06)	0.15 (0.05)	0.20 (0.05)	0.27 (0.05)	0.52 (0.04)	0.21 (0.06)	0.19 (0.04)	0.16 (0.03)
MgO	14.90 (0.19)	14.26 (0.18)	13.46 (0.13)	13.37 (0.19)	12.46 (0.14)	17.87 (0.16)	14.26 (0.15)	13.89 (0.14)	14.79 (0.55)
CaO	23.28 (0.51)	23.35 (0.50)	23.85 (0.42)	22.18 (0.53)	20.86 (0.45)	0.58 (0.11)	22.75 (0.43)	22.86 (0.19)	24.12 (0.60)
Na_2O	0.06 (0.03)	0.16 (0.03)	0.11 (0.02)	0.26 (0.04)	0.20 (0.02)	0.01 (0.01)	0.26 (0.03)	0.12 (0.03)	0.09 (0.03)
Total	98.42	100.22	98.73	98.90	98.42	99.03	99.64	98.40	100.02
Formula based on 6 oxygen atoms									
Si	1.93 (0.01)	1.97 (0.01)	1.97 (0.01)	2.00 (0.00)	1.90 (0.01)	1.98 (0.01)	1.97 (0.01)	1.95 (0.01)	1.97 (0.01)
Al^{IV}	0.03 (0.01)	0.02 (0.01)	0.02 (0.01)	0.00 (0.00)	0.07 (0.00)	0.02 (0.01)	0.03 (0.01)	0.03 (0.01)	0.02 (0.01)
Al^{VI}	0.00 (0.00)	0.00 (0.00)	0.00 (0.00)	0.03 (0.01)	0.00 (0.00)	0.03 (0.01)	0.01 (0.01)	0.00 (0.00)	0.00 (0.00)
Fe^{3+}	0.10 (0.02)	0.05 (0.02)	0.04 (0.01)	n.c.	0.13 (0.02)	n.c.	0.03 (0.02)	0.09 (0.02)	0.04 (0.01)
Cr	n.c.	0.01 (0.00)	n.c.	n.c.	0.01 (0.00)	n.c.	n.c.	n.c.	n.c.
Ti	0.00 (0.00)	0.00 (0.00)	0.00 (0.00)	0.00 (0.00)	0.00 (0.00)	0.00 (0.00)	0.00 (0.00)	0.00 (0.00)	0.00 (0.00)
Mg	0.84 (0.01)	0.79 (0.01)	0.76 (0.01)	0.75 (0.01)	0.72 (0.01)	1.03 (0.01)	0.79 (0.01)	0.79 (0.01)	0.82 (0.03)
Fe^{2+}	0.14 (0.03)	0.22 (0.04)	0.22 (0.01)	0.28 (0.02)	0.29 (0.03)	0.89 (0.01)	0.22 (0.02)	0.20 (0.01)	0.18 (0.04)
Mn	0.01 (0.00)	0.01 (0.00)	0.00 (0.00)	0.01 (0.00)	0.01 (0.00)	0.02 (0.00)	0.01 (0.00)	0.01 (0.00)	0.01 (0.00)
Ca	0.94 (0.02)	0.93 (0.02)	0.97 (0.02)	0.90 (0.02)	0.86 (0.02)	0.02 (0.00)	0.91 (0.01)	0.93 (0.01)	0.96 (0.02)
Na	0.00 (0.00)	0.01 (0.00)	0.01 (0.00)	0.02 (0.00)	0.01(0.00)	0.00 (0.00)	0.02 (0.00)	0.01 (0.00)	0.01 (0.00)
Mg#	77.25 (1.58)	74.60 (1.35)	73.92 (1.10)	72.18 (1.30)	63.79 (3.19)	53.14 (0.39)	74.94 (0.88)	72.54 (0.81)	78.72 (3.05)
$CaSiO_3$	46.44 (0.94)	46.74 (0.85)	48.48 (0.80)	46.24 (0.87)	43.46 (1.14)	1.23 (0.22)	46.21 (0.61)	46.17 (0.55)	47.99 (0.75)
$MgSiO_3$	41.36 (0.33)	39.72 (0.41)	38.08 (0.43)	38.80 (0.38)	36.04 (1.14)	52.48 (0.41)	40.30 (0.32)	39.04 (0.25)	40.93 (1.15)
$FeSiO_3$	12.20 (1.06)	13.54 (0.90)	13.44 (0.74)	14.97 (0.90)	20.50 (2.12)	46.29 (0.39)	13.48 (0.59)	14.78 (0.56)	11.09 (1.73)

[a] Not calculated (Total Fe expressed as FeO)
Mg# = [100 × Mg/(Mg + Fe^{2+} + Fe^{3+} + Mn), atomic]
Value in parentheses represents the standard deviation (1σ) of N analyses.
Abbreviation: OHP = oxide hornblende pyroxenite, FTO = Fe-Ti oxide ore, Cpx = clinopyroxene, Opx = orthopyroxene and N = number of analyzed points by EPMA

(Frost and Lindsley, 1991). These processes normally mask the initial composition of the primary Fe-Ti oxides (Buddington and Lindsley, 1964; Frost et al., 1988). The cooling of such oxides in most magmatic systems is controlled mainly by three different re-equilibration processes, namely: (1) oxide-silicate, (2) oxide-oxide, and (3) intra-oxide re-equilibration (Frost, 1991). In Mazua, microtextures and chemical variations of different types of Fe-Ti oxides suggest that the oxide hornblende pyroxenite and related Fe-Ti oxide ores experienced re-equilibration processes during cooling. Firstly, the oxide-silicate re-equilibration is indicated by very low MgO concentrations (<2 wt%) of ilmenite, which might have resulted from an ion exchange process with silicates during cooling (Frost and Lindsley, 1991). In addition, the reaction textures between ilmenite and silicates (Fig. 8e) and the very low Al_2O_3 concentrations of clinopyroxene (Fig. A.3b in ESM 1 and Table 2) might have been influenced by such re-equilibration processes. Oxide-silicate re-equilibration may cease during the last magmatic stage (700 to 950 °C, Frost, 1991; Pang et al., 2008). However, due to the presence of water fluxes mineral reactions involving amphiboles, such re-equilibration may have ended at low temperatures (400 to 500 °C, see Frost, 1991).

Secondly, in the (Ti + V) vs. Ni/(Cr + Mn) diagram of Dupuis and Beaudoin (2011), most of the magnetite grains in oxide hornblende pyroxenite and Fe-Ti oxide ores plot out of the expected composition for igneous magnetite, and into the skarn and porphyry fields, close to the boundary with the magmatic field (Fig. 13). The composition of magnetite grains in contact with ilmenite in oxide hornblende pyroxenite and Fe-Ti oxide ores is characterized by the relatively low V + Ti concentrations. The low Ti + V concentrations of magnetite suggest that the composition of magnetite was modified in subsolidus conditions. Thirdly, the intra-oxide re-equilibration is characterized by cloth-like ilmenite exsolution lamellae and magnetite-hosted trellis type spinel lamellae in oxide hornblende pyroxenite and Fe-Ti oxide ores (Fig. 7b and Fig. 8a-d). However, the contact between magnetite and ilmenite is characterized by Al-rich spinel and ilmenite lamellae, which were formed from the same mechanism as exsolution of primary titanomagnetite (Duchesne, 1972). The exsolution of such Al-rich spinel might explain the absence of correlation between the Al_2O_3 concentrations and the TiO_2 concentrations of magnetite in oxide hornblende pyroxene and related Fe-Ti oxide ores (Fig. 12d). The occurrence of coarse polygonal grains of ilmenite with well-annealed junctions suggests recrystallization of the oxides during sub-solidus conditions (Fig. 7d; Hunter, 1996). Although deformation and metamorphic overprints are not clearly expressed in the Mazua ultramafic intrusion, we cannot rule out their influence on the chemical readjustment of Fe-Ti oxides.

Oxygen fugacities (fO_2) and temperatures at which the minerals were last equilibrated are calculated based on the composition of magnetite and ilmenite pairs (Buddington and Lindsley, 1964). To avoid the effect of exsolution, pairs showing sharp contacts and those without ilmenite lamellae were chosen. The calculated subsolidus temperature and oxygen fugacities, using the QUILF program (Andersen et al., 1993), vary from 393 to 434 °C and FMQ + 1.2 to FMQ + 6.1, respectively (Table C.2 in ESM 3; FMQ = the fayalite – magnetite – quartz fO_2 buffer). The observed T-fO_2 interval may represent the last stage of the post cumulus evolution, specifically the end of subsolidus re-equilibration and exsolution (Frost, 1991) and might have been also influenced by regional metamorphism. The trend of the oxide pairs in the Mazua ultramafic intrusion is marked by increasing fO_2 associated with decreasing temperature, placing them parallel to the ilmenite isopleths (Fig. 14). This cooling path suggests that the primary oxides were mainly composed of ilmenite (Frost, 1991). In addition, the absence of hemo-ilmenite

Table 3
Compositions of different types of ilmenite in the Fe-Ti oxide ores and oxide hornblende pyroxenite from the Mazua ultramafic intrusion.

Rock Type	Fe-Ti oxide ores								Oxide hornblende pyroxenite					
Sample ID	Mzo1-st			Mzo4-lo		Mzo7-mo	Mzo17-ho		Mzo4-ho			Mzo8-ho		Mzo9-ho
Mode of occurrence	Primary	Inclusion	Secondary	Primary	Inclusion	Primary	Primary	Inclusion	Primary	Inclusion	Secondary	Primary	Inclusion	Primary
Host mineral		Cpx			Hbl			Hbl					Hbl	
N	2	6	2	32	10	20	8	18	6	11	2	43	12	10
Oxides (wt. %)														
SiO_2	<0.03	<0.03	0.08 (0.01)	0.05 (0.05)	0.05 (0.02)	0.03 (0.01)	0.04 (0.01)	0.03 (0.01)	<0.03	0.03 (0.01)	0.07 (0.00)	0.03 (0.01)	0.06 (0.06)	0.03 (0.00)
TiO_2	52.21 (0.47)	51.88 (0.27)	50.88 (0.24)	52.11 (0.33)	51.38 (0.67)	51.37 (0.40)	51.29 (0.42)	51.18 (0.37)	50.46 (0.42)	50.13 (0.49)	48.96 (0.34)	51.54 (0.35)	50.81 (0.66)	52.10 (0.34)
Al_2O_3	<0.06	<0.06	<0.06	<0.06	<0.06	<0.06	<0.06	<0.06	<0.06	<0.06	<0.06	<0.06	0.06 (0.01)	<0.06
Cr_2O_3	0.16 (0.00)	0.23 (0.00)	0.12 (0.06)	0.18 (0.07)	0.27 (0.03)	0.17 (0.01)	0.22 (0.05)	0.22 (0.06)	0.22 (0.02)	0.16 (0.02)	0.14 (0.07)	<0.15	0.18 (0.04)	<0.15
V_2O_3	0.10 (0.04)	0.11 (0.01)	<0.07	0.12 (0.05)	0.14 (0.06)	<0.07	0.17 (0.07)	0.17 (0.06)	0.20 (0.00)	0.22 (0.14)	0.16 (0.02)	0.14 (0.05)	0.19 (0.08)	<0.07
Fe_2O_3	1.59 (1.23)	1.79 (0.51)	2.29 (0.70)	1.41 (0.77)	2.32 (1.41)	2.17 (0.65)	3.14 (1.14)	3.21 (1.29)	4.18 (0.95)	4.21 (1.00)	6.53 (0.71)	1.56 (0.97)	2.71 (1.66)	0.90 (0.61)
FeO	43.16 (0.06)	42.92 (0.25)	43.16 (0.42)	43.86 (0.29)	43.60 (0.50)	42.90 (0.36)	42.48 (0.37)	42.67 (0.53)	42.85 (0.53)	42.67 (0.70)	42.12 (0.22)	44.21 (0.42)	43.71 (0.50)	44.97 (0.34)
NiO	0.09 (0.03)	0.11 (0.04)	<0.06	<0.06	0.10 (0.00)	0.06 (0.01)	0.11 (0.02)	0.10 (0.04)	0.10 (0.04)	0.16 (0.13)	<0.06	0.09 (0.02)	0.08 (0.01)	0.06 (0.00)
MnO	0.51 (0.04)	0.44 (0.07)	0.55 (0.03)	0.47 (0.08)	0.48 (0.04)	0.40 (0.05)	0.45 (0.07)	0.44 (0.07)	0.36 (0.11)	0.43 (0.10)	0.51 (0.06)	0.51 (0.07)	0.53 (0.09)	0.43 (0.07)
MgO	1.84 (0.19)	1.85 (0.03)	1.21 (0.13)	1.43 (0.04)	1.22 (0.10)	1.63 (0.05)	1.81 (0.05)	1.64 (0.16)	1.23 (0.07)	1.12 (0.19)	0.82 (0.06)	0.93 (0.12)	0.83 (0.08)	0.83 (0.04)
Total	99.66	99.33	98.29	99.63	99.56	98.73	99.69	99.67	99.29	99.13	99.31	99.01	99.16	99.31
Formula based on 3 oxygen atoms														
Si	n.c.	n.c.	0.00 (0.00)	0.00 (0.00)	0.00 (0.00)	0.0 (0.00)	0.0 (0.00)	0.0 (0.00)	n.c.	0.00 (0.00)	0.00 (0.00)	0.00 (0.00)	0.00 (0.00)	0.00 (0.00)
Ti	0.98 (0.01)	0.98 (0.00)	0.97 (0.01)	0.98 (0.01)	0.97 (0.01)	0.98 (0.01)	0.97 (0.01)	0.97 (0.01)	0.96 (0.01)	0.96 (0.01)	0.93 (0.01)	0.98 (0.01)	0.97 (0.02)	0.99 (0.01)
Al	n.c.	n.c.	n.c.	n.c.	n.c.	n.c.	n.c.	n.c.	n.c.	n.c.	n.c.	n.c.	0.00 (0.00)	n.c.
Cr	0.00 (0.00)	0.00 (0.00)	0.00 (0.00)	0.00 (0.00)	0.01 (0.00)	0.00 (0.00)	0.00 (0.00)	0.00 (0.00)	0.00 (0.00)	0.00 (0.00)	0.00 (0.00)	n.c.	0.00 (0.00)	n.c.
V	0.00 (0.00)	0.00 (0.00)	n.c.	0.00 (0.00)	0.00 (0.00)	n.c.	0.00 (0.00)	0.00 (0.00)	0.00 (0.00)	0.00 (0.00)	0.00 (0.00)	0.00 (0.00)	0.00 (0.00)	n.c.
Fe^{3+}	0.03 (0.02)	0.03 (0.01)	0.04 (0.01)	0.03 (0.01)	0.04 (0.03)	0.04 (0.01)	0.06 (0.02)	0.06 (0.02)	0.08 (0.02)	0.08 (0.02)	0.12 (0.01)	0.03 (0.02)	0.05 (0.01)	0.02 (0.01)
Fe^{2+}	0.90 (0.00)	0.90 (0.01)	0.92 (0.01)	0.92 (0.01)	0.92 (0.01)	0.91 (0.01)	0.89 (0.01)	0.89 (0.02)	0.90 (0.01)	0.91 (0.01)	0.89 (0.01)	0.94 (0.01)	0.93 (0.01)	0.95 (0.01)
Ni	0.00 (0.00)	0.00 (0.00)	n.c.	n.c.	0.00 (0.00)	0.00 (0.00)	0.00 (0.00)	0.00 (0.00)	0.00 (0.00)	0.00 (0.00)	n.c.	0.00 (0.00)	0.00 (0.00)	0.00 (0.00)
Mn	0.01 (0.00)	0.01 (0.00)	0.01 (0.00)	0.01 (0.00)	0.01 (0.00)	0.01 (0.00)	0.01 (0.00)	0.01 (0.00)	0.01 (0.00)	0.01 (0.00)	0.01 (0.00)	0.01 (0.00)	0.01 (0.00)	0.01 (0.00)
Mg	0.07 (0.01)	0.07 (0.00)	0.05 (0.00)	0.05 (0.00)	0.05 (0.00)	0.06 (0.00)	0.07 (0.00)	0.06 (0.01)	0.05 (0.00)	0.04 (0.01)	0.03 (0.00)	0.04 (0.00)	0.03 (0.01)	0.03 (0.00)
Total	2.00	2.00	2.00	2.00	2.00	2.00	2.00	2.00	2.00	2.00	2.00	2.00	2.00	2.00
Ilm (mol %)	98.22 (0.01)	98.08 (0.00)	97.69 (0.01)	98.46 (0.01)	97.54 (0.01)	97.78 (0.01)	96.64 (0.01)	96.55 (0.01)	95.82 (0.01)	95.69 (0.01)	93.48 (0.01)	98.29 (0.01)	97.12 (0.02)	99.09 (0.01)
Hem (mol %)	1.78 (0.01)	1.92 (0.00)	2.31 (0.01)	1.54 (0.01)	2.46 (0.01)	2.22 (0.01)	3.36 (0.01)	3.45 (0.01)	4.18 (0.01)	4.31 (0.01)	6.52 (0.01)	1.71 (0.01)	2.88 (0.02)	0.91 (0.01)

Sample ID	Oxide hornblende pyroxenite Mzo9-ho	Mzt10-ho		Mzo15-ho	
Mode of occurrence	Inclusion	Primary	Inclusion	Primary	Inclusion
Host mineral	Hbl		Hbl		Cpx
N	12	35	12	21	7
Oxides (wt. %)					
SiO_2	0.05 (0.00)	0.03 (0.01)	0.46 (0.80)	0.04 (0.01)	0.06 (0.01)
TiO_2	52.42 (0.35)	52.21 (0.45)	51.89 (0.57)	50.34 (0.85)	49.10 (0.32)
Cr_2O_3	<0.15	0.20 (0.05)	<0.15	0.18 (0.02)	0.21 (0.04)
V_2O_3	<0.07	0.12 (0.06)	0.12 (0.02)	0.51 (0.19)	0.46 (0.11)
Fe_2O_3	0.57 (0.31)	1.45 (0.95)	1.39 (0.60)	3.59 (1.44)	5.62 (0.62)
FeO	45.32 (0.37)	43.92 (0.91)	44.05 (0.35)	42.95 (0.82)	41.91 (0.43)
NiO	0.06 (0.00)	0.10 (0.03)	0.07 (0.00)	0.09 (0.00)	<0.06
MnO	0.47 (0.06)	0.53 (0.08)	0.53 (0.08)	0.50 (0.05)	0.49 (0.06)
MgO	0.77 (0.08)	1.41 (0.37)	1.28 (0.21)	1.04 (0.05)	1.01 (0.12)
Total	99.66	99.98	99.79	99.24	99.16
Formula based on 3 oxygen atoms					
Si	0.01 (0.00)	0.00 (0.00)	0.01 (0.02)	0.00 (0.00)	0.00 (0.00)
Ti	0.99 (0.00)	0.98 (0.01)	0.98 (0.01)	0.96 (0.02)	0.94 (0.01)
Cr	n.c.	0.00 (0.00)	n.c.	0.00 (0.00)	0.00 (0.00)
V	n.c.	0.00 (0.00)	0.01 (0.00)	0.01 (0.00)	0.01 (0.00)
Fe^{3+}	0.01 (0.01)	0.03 (0.02)	0.03 (0.01)	0.07 (0.03)	0.11 (0.01)
Fe^{2+}	0.96 (0.00)	0.92 (0.02)	0.93 (0.01)	0.91 (0.02)	0.89 (0.01)
Ni	0.01 (0.00)	0.00 (0.00)	0.00 (0.00)	0.00 (0.00)	n.c.
Mn	0.01 (0.00)	0.01 (0.00)	0.01 (0.00)	0.01 (0.00)	0.01 (0.00)
Mg	0.03 (0.00)	0.05 (0.01)	0.05 (0.01)	0.04 (0.00)	0.04 (0.00)
Total	2.00	2.00	2.00	2.00	2.00
Hem (mol %)	99.41 (0.01)	98.43 (0.01)	98.56 (0.01)	95.95 (0.01)	93.98 (0.01)
Ilm (mol %)	0.59 (0.01)	1.57 (0.01)	1.44 (0.01)	4.05 (0.01)	6.02 (0.01)

Value in parentheses represents the standard deviation (1σ) of N analyses.
Abbreviation: Cpx = clinopyroxene; Hbl = hornblende; N = number of analyzed points by EPMA and n.c. = not calculated

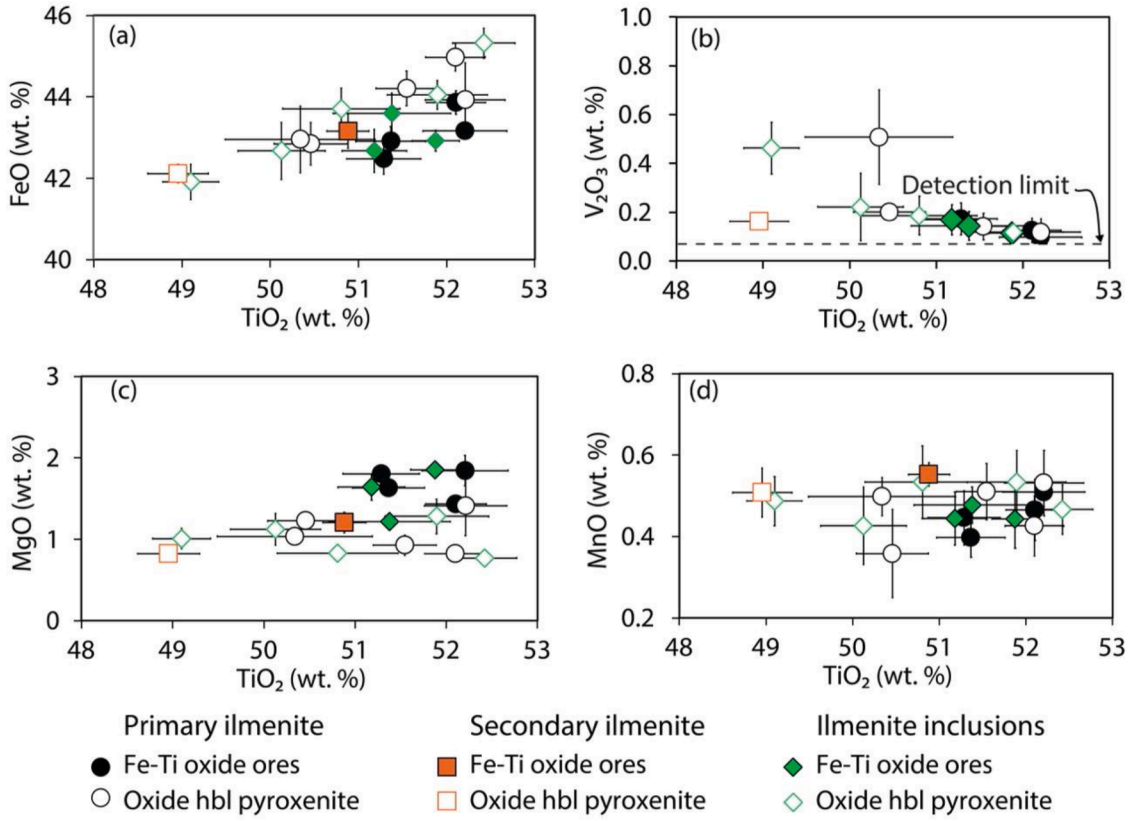

Fig. 11. (a-d) Bivariate diagrams for different types of ilmenite in oxide hornblende pyroxenite and Fe-Ti oxide ores from the Mazua intrusion. Error bars are standard deviation (1σ) and where they are not seen, the error bars are smaller than the symbols. Hlb stands for hornblende.

Table 4
Compositions of representative magnetite grains in the Fe-Ti oxide ores and oxide hornblende pyroxenite from the Mazua ultramafic intrusion.

Rock type	Fe-Ti oxide ore	Oxide hornblende pyroxenite	
Sample ID	Mzo1-st	Mzo4-ho	Mzo9-ho
N	7	9	23
Oxides (wt. %)			
SiO_2	0.05 (0.02)	0.08 (0.01)	0.05 (0.02)
TiO_2	0.12 (0.10)	0.18 (0.09)	0.30 (0.11)
Al_2O_3	0.26 (0.13)	0.26 (0.05)	0.47 (0.38)
Cr_2O_3	3.74 (0.33)	2.50 (0.25)	1.34 (0.30)
V_2O_3	2.66 (0.22)	2.21 (0.19)	1.66 (0.07)
Fe_2O_3	61.16 (0.34)	62.76 (0.84)	63.75 (0.90)
FeO	30.75 (0.32)	30.89 (0.52)	31.01 (0.19)
NiO	0.19 (0.06)	0.12 (0.05)	0.10 (0.04)
MnO	0.10 (0.01)	0.07 (0.02)	0.07 (0.03)
MgO	0.13 (0.02)	0.09 (0.03)	0.05 (0.03)
Total	99.16	99.02	98.69
Formula based on 4 oxygen atoms			
Si	0.00 (0.00)	0.00 (0.00)	0.00 (0.00)
Ti	0.00 (0.00)	0.01 (0.00)	0.01 (0.00)
Al	0.01 (0.01)	0.01 (0.00)	0.02 (0.02)
Cr	0.11 (0.01)	0.08 (0.01)	0.04 (0.01)
V	0.08 (0.01)	0.07 (0.01)	0.05 (0.00)
Fe^{3+}	1.78 (0.01)	1.83 (0.01)	1.86 (0.02)
Fe^{2+}	0.99 (0.00)	1.00 (0.01)	1.01 (0.00)
Ni	0.01 (0.00)	0.00 (0.00)	0.00 (0.00)
Mn	0.00 (0.00)	0.00 (0.00)	0.00 (0.00)
Mg	0.01 (0.00)	0.01 (0.00)	0.00 (0.00)
Total	3.00	3.00	3.00
Usp (mol %)	0.44 (0.00)	0.67 (0.00)	1.05 (0.00)
Mag (mol %)	99.56 (0.00)	99.33 (0.00)	98.95 (0.00)

Value in parentheses represents the standard deviation (1σ) of N analyses.
Abbreviation: N = number of analyzed points by EPMA.

exsolution lamellae in ilmenite at Mazua may indicate that the oxygen fugacities did not reach the ilmenite-hematite solvus during cooling (see Frost, 1991).

7.2. *Nature of the Mazua ultramafic intrusion*

The Mazua ultramafic intrusion and related Fe-Ti oxides ores differ from many ultramafic–mafic intrusions because ilmenite is the main ore mineral rather than the more common titanomagnetite (e.g. Bushveld Complex; Reynolds, 1985, Panzhihua Intrusion; Pang et al., 2008). Similar characteristics were reported in world-class anorthosite-hosted ilmenite deposits such as the Lac Tio deposit in Quebec (Charlier et al., 2015 and references therein) and Tellnes deposit in Norway (Charlier et al., 2006; Charlier et al., 2007). Small orebodies such as the Koivusaarenneva gabbro-hosted ilmenite deposit in Finland (Kärkkäinen and Bornhorst, 2003) are also noteworthy.

Textural and structural evidences support a cumulate origin of the Mazua ultramafic intrusion. Firstly, although the occurrence of classic cumulus framework of touching grains is rare due to subsolidus re-equilibration overprints, relics of cumulates textures are still preserved in some samples where straight boundaries between euhedral grains of clinopyroxene and chained euhedral ilmenite grains are common (Fig. 6a and Fig. 7e). Secondly, the presence of layering structures with alternating thin Fe-Ti oxides and silicate-rich layers is consistent with accumulation of crystals and compaction (Fig. 5a and Fig. 6c; Pang et al., 2008; Vernon and Collins, 2011; Holness, 2021). Thirdly, there are centimeter-scale structures showing silicate-rich rocks characterized by grain-size grading of clinopyroxene, indicating local physical accumulation, within some layered Fe-Ti oxide ores and oxide hornblende pyroxenite (Fig. 5a and Fig. A.1 in ESM 1; Vernon and Collins, 2011; Holness, 2021).

The primitive mantle-normalized alteration-resistant trace elements

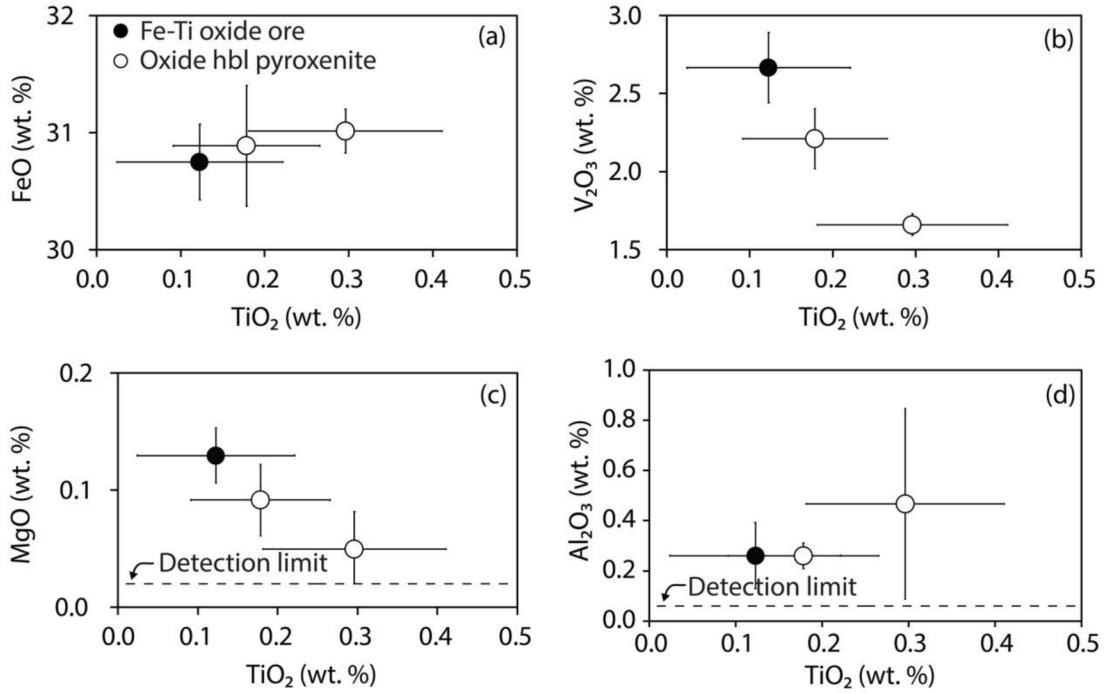

Fig. 12. Plots of (a) FeO, (b) V_2O_3, (c) MgO and (d) Al_2O_3 vs. TiO_2 of magnetite in Fe-Ti oxide ores and oxide hornblende pyroxenite from the Mazua intrusion. Error bars are 1σ. Hlb stands for hornblende.

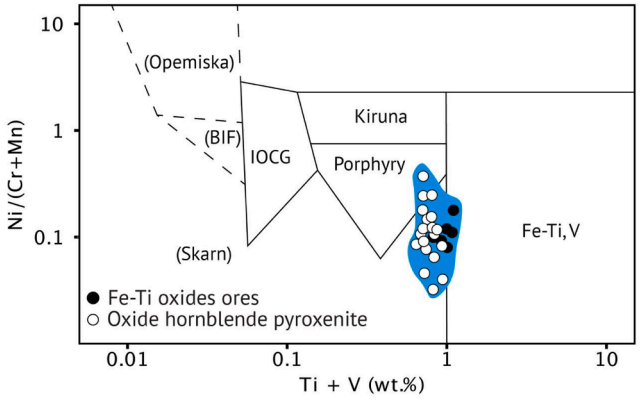

Fig. 13. Ni/(Cr + Mn) vs. Ti + V discrimination diagram of magnetite in Fe-Ti oxide ores and oxide hornblende pyroxenite of the Mazua intrusion (adapted from Dupuis and Beaudoin, 2011). The compositions of magnetite from the Mazua intrusion are compared with the average compositions of magnetite from different types of deposits [iron oxide-copper–gold (IOCG), Kiruna-type apatite-magnetite, banded iron formation (BIF), porphyry, Fe-Cu skarn, ortho-magmatic Fe-Ti, V and Opemiska-type Cu veins].

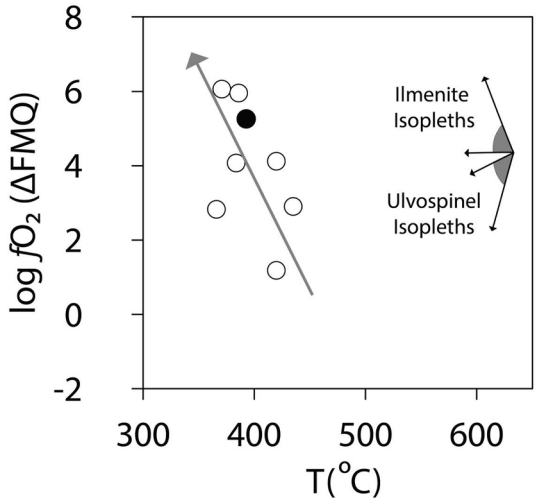

Fig. 14. A plot of re-equilibration temperatures and oxygen fugacities calculated from representative magnetite–ilmenite pairs of oxide hornblende pyroxenite and Fe-Ti oxide ore from the Mazua ultramafic intrusion using the QUILF program (Andersen et al., 1993). Oxygen fugacities are normalized to that of the FMQ buffer at the same pressure and temperature [$\log fO_2(\Delta FMQ) = \log fO_2 - \log fO_2(FMQ)$]. Directions of ilmenite and ulvospinel isopleths towards lower temperatures (after Frost, 1991). The open and filled circles stand for oxide hornblende pyroxenite and Fe-Ti oxide ore, respectively. Abbreviation: FMQ: fayalite–magnetite–quartz

patterns are characterized by pronounced positive anomalies of Ta, Nb and Ti, which are especially pronounced in the Fe-Ti-rich ore samples (Fig. 10). The concentrations of Ti, Nb and Ta are positively correlated with each other and, given the well-known compatibility of Nb and Ta in Ti-oxides, their enrichment is likely associated with their high distribution coefficients in these oxides (Klemme et al., 2006; Plavsa et al., 2018).

The occurrence of the cumulate assemblage (clinopyroxene + ilmenite ± magnetite) in the Mazua ultramafic intrusion suggests that the magma had undergone differentiation before its emplacement. The evolved nature of the intrusion is consistent with the fractionation of plagioclase prior to the emplacement of the Mazua intrusion due to its absence in the studied samples. The segregation and accumulation of plagioclase would have formed a plagioclase-rich rock, such as anorthosite, which remains so far unidentified in Mazua (Cílek, 1989). The early saturation of plagioclase from a basaltic melt can be attributed to the reduction of the pressure of the magma chamber, which expands the stability field of plagioclase (Naslund and McBirney, 1996; Cawthorn, 2003; Cawthorn and Ashwal, 2009; Latypov et al., 2020). As a result of the decompression, the melt is supersaturated with plagioclase, which is crystallized alone (Cawthorn and Ashwal, 2009). In addition,

plagioclase can be segregated from the coprecipitating phases (ilmenite and clinopyroxene) due to its buoyant nature in basaltic magmas (Miller and Weiblen, 1990; Charlier et al., 2007; Charlier et al., 2009; Charlier et al., 2015); such a process would lead to the vertical floatation of plagioclase, due to differences in density, and the formation of an anorthosite body at the upper part of the Mazua ultramafic intrusion, which might have been later eroded. A similar mechanism is plausible in Mazua, despite the lack of evidence to support it. Our unpublished whole-rock composition data of two samples of amphibolite enclaves at Mazua (Fig. 4d) suggest that they might represent relicts of a possible mafic body of the intrusion.

Since chilled margins of the Mazua ultramafic intrusion are not easily recognizable as the rocks rarely crop out, spatially related dikes or sills are still unknown, and melt inclusions were not identified in the ore-bearing rocks, the melt composition was estimated based on the clinopyroxene-liquid equilibrium, following the method applied by Bai et al. (2014). The average Fe-Mg partition coefficient [$Kd_{cpx/melt} = (FeO/MgO)_{cpx}/(FeO/MgO)_{melt}$] of 0.27 (Bédard, 2010) and the composition of most primitive clinopyroxene, with Mg-number varying from 74 to 82, in the oxide hornblende pyroxenite were used to calculate the composition of the coexisting melt. The calculated Mg-number of the melt varies from 44 to 55, consistent with the evolved nature of the melt, and is relatively close to those of the Panzhihua and Skaergaard intrusions (a comparison of Mg-numbers of many other well-known Fe-Ti oxides-bearing intrusions is shown in Table C.3; ESM 3). Since the chemical composition of clinopyroxene grains in Mazua varies widely, suggesting a significant effect of re-equilibration processes, the cores of most primitive grains without recrystallization textures were used for the calculation.

7.3. Fe-Ti oxides saturation and ore-forming processes

In the last 70 years, petrologists have addressed several mechanisms responsible for the formation of Fe-Ti oxide deposits hosted in mafic–ultramafic massifs and anorthosites around the world. Such mechanisms include (1) liquid immiscibility (Reynolds, 1985; Duchesne, 1999; Zhou et al., 2005), (2) settling and sorting of Fe-Ti oxide minerals (Pang et al., 2008; Cawthorn and Ashwal, 2009; Charlier et al., 2009), (3) magma recharge and mixing (Irvine, 1977; Bai et al., 2012), (4) variation of the oxidation state in the magma (Klemm et al., 1985) and (5) variation of the pressure (Cawthorn and Ashwal, 2009). The first two mechanisms are the most accepted among researchers.

Liquid immiscibility involves the phase separation of an evolving magma into Fe-Ti rich and silica-rich immiscible liquids (Cawthorn and Ashwal, 2009). Despite the lack of experimental data, field and textural observations have been used to support the existence of Fe-Ti rich melts immiscible with silicate melts (Lindsley and Epler, 2017). Zhou et al. (2005) suggested that the oxide layers in the Panzhihua Intrusion were formed by an immiscible Fe-Ti rich liquid that was separated from a Fe-Ti rich mafic silicate magma. To support the model, they noted the occurrence of Fe-Ti oxides that fill interstices between, or completely enclose, silicate minerals, implying a percolation of a dense and low-viscosity Fe-rich liquid through silicate crystal mush. However, textures suggesting an “invasion” of such melts and embayed texture associated with amphibole rims around other silicates were not observed in the Mazua ultramafic intrusion. Instead, textures in Mazua suggest that Fe-Ti oxides and pyroxenes formed simultaneously in the oxide hornblende pyroxenite and Fe-Ti oxide ores, which is supported by the positive correlation between MgO concentrations of ilmenite and Mg-numbers of clinopyroxene (Fig. A.4 in ESM 1). Interstitial Fe-Ti oxides in the Mazua samples (Fig. 6a-b) seem to be a consequence of subsolidus grain boundary readjustment. Curved oxide-silicate boundaries may be formed due to the tendency of oxides to wet silicate boundaries during subsolidus re-equilibration (Duchesne, 1999; Pang et al., 2008). One of the other points that argues against Fe-Ti melt immiscibility is the scarcity of phosphorus-bearing minerals such as apatite in all the samples, with the exception of Mzo7-ho, supported by the whole-rock composition characterized by extremely low whole-rock P_2O_5 concentrations of the oxide hornblende pyroxenite and the Fe-Ti oxide ores (Table 1). Fe-rich liquids are usually more enriched in phosphorus in comparison to silicate magmas (Watson, 1976; Troll et al., 2019). Considerable amounts of phosphorus-bearing minerals are expected to crystallize from such melts, which is not the case of the Mazua ultramafic intrusion. Strong evidence in favor of immiscible Fe-Ti oxide melts is the cross-cutting relationship between oxide bodies and their host rocks (Charlier et al., 2015; Lindsley and Epler, 2017). Cross-cutting structures locally occur as very small-scale veins in the intrusive rocks of the Mazua ultramafic intrusion (Fig. 4b), but due to their very restricted occurrence, we argue that Fe-Ti melt immiscibility was not an important mechanism for the formation of the entire volume of Fe-Ti oxide ores in Mazua. In contrast, settling and sorting are likely to be the most plausible mechanism that produced Fe-Ti oxides ores in the Mazua ultramafic intrusion. The occurrence of thin Fe-Ti oxide ore layers alternating with oxide hornblende pyroxenite, in almost every studied location, and the sharp contact between them are explained by gravitational settling and sorting of Fe-Ti oxides (Fig. 5a; Pang et al., 2008). Density differences between the early formed Fe-Ti oxides (>4.5 g/cm^3) and silicate magma (<3.5 g/cm^3) influence the quick sinking of oxides onto the bottom of the magma chamber, followed by other silicate minerals, such as pyroxenes, to form the overlying layers (Pang et al., 2008; Bai et al., 2012).

An experimental study by Toplis and Carroll (1995) showed that the timing of ilmenite crystallization is mainly controlled by the TiO_2 concentration of the magma rather than oxidation state. Under common geological conditions, ilmenite and magnetite are present on the liquidus together with clinopyroxene when the TiO_2 concentration in the magma is over 4 wt% (Bai et al., 2014 and references therein). On the other hand, titanomagnetite is present on the liquidus with clinopyroxene when the TiO_2 concentration is lower than 4 wt% (Bai et al., 2014 and references therein). In the Mazua intrusion, ilmenite comprises 97 vol% of the Fe-Ti oxides (with very low abundance of magnetite) in oxide hornblende pyroxenite and related ores, and it coexists with clinopyroxene, which suggests the TiO_2 concentration of the magma of >4 wt%. High TiO_2 concentration of the magma was suggested for the Tellnes ilmenite deposit by Charlier et al. (2006) and the Svecofennian Koivusaarenneva Gabbro by Kärkkäinen and Bornhorst (2003).

Regarding the origin of the Fe-Ti rich silicate melt, it is unlikely that the mantle-derived basaltic melt was already enriched in Fe and Ti and that the saturation of ilmenite occurred at very early stages of differentiation, prior to the emplacement of the Mazua ultramafic intrusion. Moreover, the fact that the Mesoproterozoic Nampula Block was formed in a subduction tectonic framework (Macey et al., 2010) cannot rule out the influence of the subducted slab component on the composition of the parental magma of the Mazua intrusion. However, no evidence exists to support the enrichment in Fe-Ti in the slab. In addition, there is no evidence of the existence of Fe-Ti rich country rocks in the region that would be assimilated by the magma during its ascent. Therefore, we argue that the enrichment of Ti and Fe in the ore-bearing pyroxenites at Mazua may be explained by the fractionation processes, namely the segregation of plagioclase and possibly olivine (indicated by its absence in all the samples, with the exception of Mzo8-ho, and relative low whole-rock Ni concentrations; Table 1) before the emplacement of the Mazua ultramafic intrusion leading to a formation of Fe-Ti enriched silicate liquid. Sorting and accumulation of Fe-Ti oxides onto the bottom of the magma chamber, after co-precipitation of the minerals from the Fe-Ti enriched magma, would have enhanced the formation of high-grade ilmenite layers in the Mazua ultramafic intrusion.

7.4. The potential of ilmenite ore for beneficiation

The ilmenite orebody from the Mazua ultramafic intrusion may be suitable for the industrial production of pigment, despite its limited

spatial distribution. The industrial processing of ilmenite is very sensitive to the major and trace elements composition, especially to the Cr and Mg impurities (Charlier et al., 2007). High concentrations of Mg and Cr in ilmenite affect negatively the chlorination and sulfatation processes often used in the TiO_2 pigment industry for beneficiation (Chernet, 1999; Duchesne and Vander Auwera, 2001; Charlier et al., 2015). The ilmenite at Mazua is almost pure (Geological Institute Belgrade, 1984). It is characterized by low concentrations of MgO (<1.9 wt%) and Cr_2O_3 (<0.3 wt%), a fact that enhances its potential for beneficiation (Table 3). As previously discussed, Fe-Ti oxides at Mazua underwent substantial subsolidus re-equilibration during cooling. As this process takes place, primary ilmenite reduces its hematite and hercynite concentrations and magnetite tends to lose Ti, Al and Mg through external granule exsolution of spinelliferous ilmenite (Pang et al., 2008, Charlier et al., 2015). Consequently, primary ilmenite and magnetite approach to their pure end-member compositions and their minor elements (impurities) are removed (Pang et al., 2008; Charlier et al., 2015). At Mazua, the hematite component in the primary ilmenite does not exceed 4 mol % (Table 3) and might have been controlled by subsolidus processes, improving, therefore, the industrial value of the ilmenite orebody.

8. Conclusions

The Mazua ultramafic intrusion is composed of oxide-hornblende pyroxenite and Fe-Ti oxide ores and trends E-W concordantly with the banded biotite gneiss country rock. The rocks of the Mazua intrusion are mainly composed of clinopyroxene, Fe-Ti oxides and magmatic amphibole. The main ore mineral is ilmenite, which occurs either as monomineralic aggregates in the Fe-Ti oxide ores or interstitial fillings in the oxide hornblende pyroxenite. Ilmenite constitutes 97 vol% of the Fe-Ti oxides, and its abundance controls the variations in the whole-rock FeO_{Total} and TiO_2 concentrations of the oxide-bearing rocks and ores.

The textural and structural data presented here support a cumulate origin for the Mazua ultramafic intrusion. Moreover, the evolved geochemical nature of the magma is indicated by (1) the observed mineral assemblage (clinopyroxene + ilmenite ± magnetite, without plagioclase and olivine in all the samples, with the exception of Mzo8-ho) and (2) the calculated low Mg-number of the melt of approximately 50. These geochemical characteristics indicate the early crystallization and segregation of plagioclase, suggesting the existence of an early formed body of anorthosite, which remains so far unidentified.

Settling and sorting are suggested to be the main mechanisms that formed Fe-Ti oxide ores in the Mazua ultramafic intrusion. Microtextures and chemical variations of different types of Fe-Ti oxides suggest that the rocks from Mazua were subjected to extensive subsolidus re-equilibration processes during cooling.

Declaration of Competing Interest

The authors declare that they have no known competing financial interests or personal relationships that could have appeared to influence the work reported in this paper.

Acknowledgments

This research was supported by the KIZUNA Program of the Japan International Cooperation Agency (JICA). We thank Mr. Mauricio Meliva for providing fieldwork assistance. We greatly thank Professor Shoji Arai, Professor Lewis D. Ashwal and Professor B. Ronald Frost for the constructive comments on the initial draft of the manuscript which helped to improve its clarity. We are indebted to Dr. Kotaro Yonezu, Dr. Thomas Tindell, Dr. Takuya Echigo and Dr. Jacob Kaavera for their constructive suggestions and discussion at various stages during the preparation of the manuscript. Discussion with members of the Economic Geology Laboratory from Akita and Kyushu Universities helped to consolidate our thinking on Fe-Ti oxide magmatic deposits.

Appendix A. Supplementary data

Supplementary data to this article can be found online at https://doi.org/10.1016/j.oregeorev.2022.104760.

References

Andersen, D.J., Lindsley, D.H., Davidson, P.M., 1993. QUILF: A pascal program to assess equilibria among Fe-Mg-Mn-Ti oxides, pyroxenes, olivine, and quartz. Comput. Geosci. 19 (9), 1333–1350. https://doi.org/10.1016/0098-3004(93)90033-2.

Bai, Z.J., Zhong, H., Naldrett, A.J., Zhu, W.G., Xu, G.W., 2012. Whole-rock and mineral composition constraints on the genesis of the giant Hongge Fe-Ti-V oxide deposit in the Emeishan Large Igneous Province, Southwest China. Econ. Geol. 107 (3), 507–524. https://doi.org/10.2113/econgeo.107.3.507.

Backeberg, N.R., 2015. Damaged Goods: Regional deformation history and structural controls on the Hammond Reef gold deposit, Atikokan, Ontario. McGill University (Canada).

Bai, Z.J., Zhong, H., Li, C., Zhu, W.G., He, D.F., Qi, L., 2014. Contrasting parental magma compositions for the Hongge and Panzhihua magmatic Fe-Ti-V oxide deposits, Emeishan Large Igneous Province, SW China. Econ. Geol. 109 (6), 1763–1785. https://doi.org/10.2113/econgeo.109.6.1763.

Barnes, S.J., Mole, D.R., Le Vaillant, M., Campbell, M.J., Verrall, M.R., Roberts, M.P., Evans, N.J., 2016. Poikilitic textures, heteradcumulates and zoned orthopyroxenes in the Ntaka Ultramafic Complex, Tanzania: implications for crystallization mechanisms of oikocrysts. J. Petrol. 57 (6), 1171–1198. https://doi.org/10.1093/petrology/egw036.

Barr, M.W.C., Brown, M.A., 1987. Precambrian gabbro–anorthosite complexes, Tete Province, Mozambique. Geological Journal 22 (2), 139–159. https://doi.org/10.1002/gj.3350220612.

Bédard, J.H., 2010. Parameterization of the Fe-Mg exchange coefficient (Kd) between clinopyroxene and silicate melts. Chem. Geol. 274 (3–4), 169–176. https://doi.org/10.1016/j.chemgeo.2010.04.003.

Buddington, A.F., Lindsley, D.H., 1964. Iron-titanium oxide minerals and synthetic equivalents. J. Petrol. 5 (2), 310–357. https://doi.org/10.1093/petrology/5.2.310.

Buseck PR, Nord Jr GL, Veblen DR (1980) Subsolidus phenomena in pyroxenes. In Prewitt CT (Ed.), Pyroxenes, Reviews in Mineralogy, 7, 117-211.

Carmichael, I.S., 1967. The iron-titanium oxides of salic volcanic rocks and their associated ferromagnesian silicates. Contrib. Miner. Petrol. 14 (1), 36–64. https://doi.org/10.1029/JZ072i018p04665.

Cawthorn, R.G., 2003. Genesis of magmatic oxide deposits – a view from the Bushveld Complex. Norges Geologiske Undersøkelse, Special Publication 9, 11–20.

Cawthorn, R.G., Ashwal, L.D., 2009. Origin of anorthosite and magnetite layers in the Bushveld Complex, constrained by major element compositions of plagioclase. J. Petrol. 50 (9), 1607–1637. https://doi.org/10.1093/petrology/egp042.

Charlier, B., Duchesne, J.C., Vander Auwera, J., 2006. Magma chamber processes in the Tellnes ilmenite deposit (Rogaland Anorthosite Province, SW Norway) and the formation of Fe–Ti ores in massif-type anorthosites. Chem. Geol. 234 (3–4), 264–290. https://doi.org/10.1016/j.chemgeo.2006.05.007.

Charlier, B., Skår, Ø., Korneliussen, A., Duchesne, J.C., Vander Auwera, J., 2007. Ilmenite composition in the Tellnes Fe–Ti deposit, SW Norway: fractional crystallization, postcumulus evolution and ilmenite–zircon relation. Contrib. Miner. Petrol. 154 (2), 119–134. https://doi.org/10.1007/s00410-007-0186-8.

Charlier, B., Namur, O., Duchesne, J.C., Wiszniewska, J., Parecki, A., Auwera, J.V., 2009. Cumulate origin and polybaric crystallization of Fe-Ti oxide ores in the Suwalki anorthosite, northeastern Poland. Econ. Geol. 104 (2), 205–221. https://doi.org/10.2113/gsecongeo.104.2.205.

Charlier, B., Namur, O., Bolle, O., Latypov, R., Duchesne, J.C., 2015. Fe–Ti–V–P ore deposits associated with Proterozoic massif-type anorthosites and related rocks. Earth Sci. Rev. 141, 56–81. https://doi.org/10.1016/j.earscirev.2014.11.005.

Chernet T (1999) Effect of mineralogy and texture in the TiO_2 pigment production process of the Tellnes ilmenite concentrate. Mineralogy and petrology, 67(1-2), 21-32. 10.1007/BF01165113.

Cílek, V., 1989. Industrial Minerals of Mozambique. Ministry of Mineral Resources, National Geological Institute, Mozambique, Czech Geological Office, p. 326.

Droop, G.T.R., 1987. A general equation for estimating Fe^{3+} concentrations in ferromagnesian silicates and oxides from microprobe analyses, using stoichiometric criteria. Mineral. Mag. 51 (361), 431–435. https://doi.org/10.1180/minmag.1987.051.361.10.

Duchesne, J.C., 1972. Iron-titanium oxide minerals in the Bjerkrem-Sogndal Massif, South-western Norway. J. Petrol. 13 (1), 57–81. https://doi.org/10.1093/petrology/13.1.57.

Duchesne, J.C., 1999. Fe-Ti deposits in Rogaland anorthosites (South Norway): geochemical characteristics and problems of interpretation. Miner. Deposita 34 (2), 182–198. https://doi.org/10.1007/s001260050195.

Duchesne, J.C., Vander Auwera, J., 2001. Ti deposits in anorthosite: geochemical constraints on the economic value. In Proceedings of the Biennial SGA Meeting 6, 569–571.

Dupuis, C., Beaudoin, G., 2011. Discriminant diagrams for iron oxide trace element fingerprinting of mineral deposit types. Miner. Deposita 46 (4), 319–335. https://doi.org/10.1007/s00126-011-0334-y.

Engvik, A.K., Tveten, E., Bingen, B., Viola, G., Erambert, M., Feito, P., De Azavedo, S., 2007. P-T–t evolution and textural evidence for decompression of Pan-African high-pressure granulites, Lurio Belt, north-eastern Mozambique. J. Metamorph. Geol. 25 (9), 935–952. https://doi.org/10.1111/j.1525-1314.2007.00736.x.

Engvik, A.K., Tveten, E., Solli, A., 2019. High-grade metamorphism during Neoproterozoic to Early Palaeozoic Gondwana assembly, exemplified from the East African Orogen of northeastern Mozambique. J. Afr. Earth Sc. 151, 490–505. https://doi.org/10.1016/j.jafrearsci.2018.12.021.

Evans, R.J., Ashwal, L.D., Hamilton, M.A., 1999. Mafic, ultramafic, and anorthositic rocks of the Tete Complex, Mozambique: petrology, age, and significance. S. Afr. J. Geol. 102 (2), 153–166. https://hdl.handle.net/10520/EJC-11159bc8bb.

Fritz, H., Abdelsalam, M., Ali, K.A., Bingen, B., Collins, A.S., Fowler, A.R., Ghebreab, W., Hauzenberger, C.A., Johnson, P.R., Kusky, T.M., Macey, P., Muhongo, S., Stern, R.J., Viola, G., 2013. Orogen styles in the East African Orogen: a review of the Neoproterozoic to Cambrian tectonic evolution. J. Afr. Earth Sc. 86, 65–106. https://doi.org/10.1016/j.jafrearsci.2013.06.004.

Frost, B.R., Lindsley, D.H., Andersen, D.J., 1988. Fe-Ti oxide-silicate equilibria: assemblages with fayalitic olivine. Am. Mineral. 73 (7–8), 727–740.

Frost BR (1991) Magnetic petrology: factors that control the occurrence of magnetite in crustal rocks. In: Lindsley DH (Ed.), Oxide Minerals: Petrologic and Magnetic Significance, Reviews in Mineralogy, 25, 489-509.

Frost BR, Lindsley DH (1991) Occurrence of iron-titanium oxides in igneous rocks. In: Lindsley DH (Ed.), Oxide Minerals: Petrologic and Magnetic Significance, Reviews in Minerology, 25, 433-450.

Geological Institute Belgrade, 1984. Final report on geology investigations of asbestos, iron minerals, apatite and amazonite (Localities: Alua – Nacala-a-Velha, Serra Meluli and Serra Namuhuca) in Nampula Province. National Directorate for Geology, Ministry of Mineral Resources, Mozambique.

Gillis, K.M., Meyer, P.S., 2001. Metasomatism of oceanic gabbros by late stage melts and hydrothermal fluids: Evidence from the rare earth element composition of amphiboles. Geochem. Geophys. Geosyst. 2 (3) https://doi.org/10.1029/2000GC000087.

Grantham, G.H., Marques, J.M., Wilson, M.G.C., Manhiça, V., Hartzer, F.J., 2011. Explanation of the geological map of Mozambique, scale 1: 1 000 000. Direcção Nacional de Geologia, Ministério dos Recursos Minerais, República de Moçambique, Maputo, Mozambique, p. 383.

GTK Consortium (2006) Map Explanation; Volume 4: Sheets 1430–1432 and 1530–1534. Geology of Degree Sheets Inhamambo, Maluwera, Chifunde, Zumbo, Fíngoè-Mágoè, Songo, Cazula and Zóbuè, Mozambique. Direcção Nacional de Geologia (DNG), Maputo.

Holness, M.B., 2021. In: Encyclopedia of Geology. Elsevier, pp. 99–112. https://doi.org/10.1016/B978-0-12-409548-9.12460-1.

Hunter RH (1996) Textural development in cumulate rocks. In: Cawthorn RG (Ed.), Layered Intrusions: Developments in Petrology, Elsevier, 15, 77-101.

Imai, N., Terashima, S., Itoh, S., Ando, A., 1995. 1994 Compilation of analytical data for minor and trace elements in seventeen GSJ geochemical reference samples, "Igneous rock series". Geostandards Newsletter 19 (2), 135–213. https://doi.org/10.1111/j.1751-908X.1995.tb00158.x.

Irvine, T.N., 1977. Origin of chromitite layers in the Muskox intrusion and other stratiform intrusions: A new interpretation. Geology 5 (5), 273–277. https://doi.org/10.1130/0091-7613(1977)5<273:OOCLIT>2.0.CO;2.

Jacobs, J., Fanning, C.M., Henjes-Kunst, F., Olesch, M., Paech, H.J., 1998. Continuation of the Mozambique Belt into East Antarctica: Grenville-age metamorphism and polyphase Pan-African high-grade events in central Dronning Maud Land. J. Geol. 106 (4), 385–406. https://doi.org/10.1086/516031.

Kärkkäinen, N., Bornhorst, T., 2003. The Svecofennian gabbro-hosted Koivusaarenneva magmatic ilmenite deposit, Klvi. Finland. Mineralium Deposita 2 (38), 169–184. https://doi.org/10.1007/s00126-002-0297-0.

Klemm, D.D., Henckel, J., Dehm, R.M., Von Gruenewaldt, G., 1985. The geochemistry of titanomagnetite in magnetite layers and their host rocks of the eastern Bushveld Complex. Econ. Geol. 80 (4), 1075–1088. https://doi.org/10.2113/gsecongeo.80.4.1075.

Klemme, S., Günther, D., Hametner, K., Prowatke, S., Zack, T., 2006. The partitioning of trace elements between ilmenite, ulvospinel, armalcolite and silicate melts with implications for the early differentiation of the moon. Chem. Geol. 234 (3–4), 251–263. https://doi.org/10.1016/j.chemgeo.2006.05.005.

Kröner, A., Stern, R.J., 2004. Pan-African Orogeny. Encyclopedia of. Geology 1, 1–12. https://doi.org/10.1016/B0-12-369396-9/00431-7.

Lächelt S (2004) Geology and Mineral Resources of Mozambique. Direcção Nacional de Geologia Moçambique, 515 pp.

Latypov, R., Chistyakova, S., Costin, G., Namur, O., Barnes, S., Kruger, W., 2020. Monomineralic anorthosites in layered intrusions are indicators of the magma chamber replenishment by plagioclase-only-saturated melts. Sci. Rep. 10 (1), 1–14. https://doi.org/10.1038/s41598-020-60778-w.

Lindsley, D.H., Epler, N., 2017. Do Fe-Ti-oxide magmas exist? Probably not! Am. Mineral. 102 (11), 2157–2169. https://doi.org/10.2138/am-2017-6091.

Macey, P.H., Thomas, R.J., Grantham, G.H., Ingram, B.A., Jacobs, J., Armstrong, R.A., Roberts, M.P., Bingen, B., Hollick, L., de Kock, G.S., Viola, G., Bauer, W., Gonzales, E., Bjerkgård, T., Henderson, I.H.C., Sandstad, J.S., Cronwright, M.S., Harley, S., Solli, A., Nordgulen, Ø., Motuza, G., Daudi, E., Manhiça, V., 2010. Mesoproterozoic geology of the Nampula Block, northern Mozambique: tracing fragments of Mesoproterozoic crust in the heart of Gondwana. Precambr. Res. 182 (1–2), 124–148. https://doi.org/10.1016/j.precamres.2010.07.005.

Mandlaze, J.D., 2013. Petrologia e Mapeamento Geológico em Escala 1: 10 000 no Distrito de Memba, Localidade de Mazua. Província de Nampula. Unpublished BSc, Thesis, Eduardo Mondlane University, p. 60.

Meert, J.G., 2003. A synopsis of events related to the assembly of eastern Gondwana. Tectonophysics 362 (1–4), 1–40. https://doi.org/10.1016/S0040-1951(02)00629-7.

Milani, L., Bolhar, R., Cawthorn, R.G., Frei, D., 2017. In situ LA–ICP-MS and EPMA trace element characterization of Fe–Ti oxides from the phoscorite–carbonatite association at Phalaborwa, South Africa. Mineralium Deposita 52 (5), 747–768. https://doi.org/10.1007/s00126-016-0696-2.

Miller Jr, J.D., Weiblen, P.W., 1990. Anorthositic rocks of the Duluth Complex: examples of rocks formed from plagioclase crystal mush. J. Petrol. 31 (2), 295–339. https://doi.org/10.1093/petrology/31.2.295.

Naslund HR, McBirney AR (1996) Mechanisms of formation of igneous layering. In: Cawthorn RG (Ed.), Layered Intrusions: Developments in Petrology. Elsevier, 15, 1-44. 10.1016/S0167-2894(96)80003-0.

Norconsult Consortium, 2007. Mineral Resources Management Capacity Building Project, Republic of Mozambique; Component 2: Geological Infrastructure Development Project, Geological Mapping Lot 1; Sheet Explanation: 32 Sheets; Scale: 1/250000, Report No. B6. National Directorate of Geology, Republic of Mozambique, p. 778.

Pang, K.N., Zhou, M.F., Lindsley, D.H., Zhao, D., Malpas, J., 2008. Origin of Fe-Ti Oxide ores in mafic intrusions: evidence from the Panzhihua Intrusion, SW China. J. Petrol. 49 (2), 295–313. https://doi.org/10.1093/petrology/egm082.

Plavsa, D., Reddy, S.M., Agangi, A., Clark, C., Kylander-Clark, A., Tiddy, C.J., 2018. Microstructural, trace element and geochronological characterization of TiO_2 polymorphs and implications for mineral exploration. Chem. Geol. 476, 130–149. https://doi.org/10.1016/j.chemgeo.2017.11.011.

Reynolds, I.M., 1985. Contrasting mineralogy and textural relationships in the uppermost titaniferous magnetite layers of the Bushveld complex in the Bierkraal area north of Rusternburg. Econ. Geol. 80 (4), 1027–1048. https://doi.org/10.2113/gsecongeo.80.4.1027.

Stern, R.J., 1994. Arc assembly and continental collision in the Neoproterozoic East African Orogen: implications for the consolidation of Gondwanaland. Annual Reviews Earth and Planetary Sciences 22 (1), 319–351. https://doi.org/10.1146/annurev.ea.22.050194.001535.

Sun, S.S., McDonough, W.F., 1989. Chemical and isotopic systematics of oceanic basalts: implications for mantle composition and processes. Geological Society (London), Special Publications 42 (1), 313–345. https://doi.org/10.1144/GSL.SP.1989.042.01.19.

Thomas, R.J., Jacobs, J., Horstwood, M.S.A., Ueda, K., Bingen, B., Matola, R., 2010. The Mecubúri and Alto Benfica Groups, NE Mozambique: Aids to unravelling ca. 1 and 0.5 Ga events in the East African Orogen. Precambr. Res. 178 (1–4), 72–90. https://doi.org/10.1016/j.precamres.2010.01.010.

Toplis, M.J., Carroll, M.R., 1995. An experimental study of the influence of oxygen fugacity on Fe-Ti oxide stability, phase relations, and mineral – melt equilibria in ferro-basaltic systems. J. Petrol. 36 (5), 1137–1170. https://doi.org/10.1093/petrology/36.5.1137.

Troll, V.R., Weis, F.A., Jonsson, E., Andersson, U.B., Majidi, S.A., Högdahl, K., Harris, C., Millet, M.A., Chinnasamy, S.S., Kooijman, E., Nilsson, N.P., 2019. Global Fe–O isotope correlation reveals magmatic origin of Kiruna-type apatite-iron-oxide ores. Nat. Commun. 10 (1), 1712. https://doi.org/10.1038/s41467-019-09244-4.

Unganai, D.A.B., 2019. Geochemistry and Petrogenesis of the Mazua Ultramafic Massif, Northern Mozambique: Constraints on the Associated Fe-Ti Oxide Deposit. Unpublished MSc, Thesis, Akita University, p. 166.

Vernon, R.H., Collins, W.J., 2011. Structural criteria for identifying granitic cumulates. J. Geol. 119 (2), 127–142. https://doi.org/10.1086/658198.

Viola, G., Henderson, I.H.C., Bingen, B., Thomas, R.J., Smethurst, M.D., De Azavedo, S., 2008. Growth and collapse of a deeply eroded orogen: Insights from structural, geophysical, and geochronological constraints on the Pan-African evolution of NE Mozambique. Tectonics 27. https://doi.org/10.1029/2008TC002284.

Watson, E.B., 1976. Two-liquid partition coefficients: experimental data and geochemical implications. Contrib. Miner. Petrol. 56 (1), 119–134. https://doi.org/10.1007/BF00375424.

Westerhof, A.P., Tahon, A., Koistinen, T., Lehto, T., Åkerman, C., 2008. Igneous and tectonic setting of the allochthonous Tete Gabbro-Anorthosite Suite, Mozambique. Geol. Surv. Finland 48, 191–210.

Zhou, M.F., Robinson, P.T., Lesher, C.M., Keays, R.R., Zhang, C.J., Malpas, J., 2005. Geochemistry, petrogenesis, and metallogenesis of the Panzhihua gabbroic layered intrusion and associated Fe-Ti-V oxide deposits, Sichuan Province, SW China. J. Petrol. 46 (11), 2253–2280. https://doi.org/10.1093/petrology/egi054.